PHYSICAL REVIEW C **89**, 025807 (2014)

Explosive nucleosynthesis of ^{15}N in a massive-star model

Michael J. Bojazi and Bradley S. Meyer
Department of Physics and Astronomy, Clemson University, Clemson, South Carolina 29634, USA
(Received 28 October 2013; published 21 February 2014)

Background: Presolar meteoritic graphite grains from supernovas show spatially correlated excesses in ^{15}N and ^{18}O. These excesses signal the helium-rich layers of supernova ejecta as important source material for the grains.
Purpose: Elucidate the explosive nucleosynthesis of ^{15}N in massive stars, especially during shock passage through the helium-rich stellar layers.
Method: A simple but realistic model of shock passage through the outer layers of exploding massive stars is used to follow the important ^{15}N nucleosynthesis production pathways and their sensitivity to explosion energy and governing reaction rates in a particular stellar model. All calculations are performed with open-source, freely available codes.
Results: Recent reaction rate updates tend to decrease by $\sim 4\times$ the explosive helium-burning yield of ^{15}N relative to some commonly used stellar model outputs.
Conclusions: Neutron-capture reactions on ^{18}F play an important role in the explosive production of ^{15}N in helium-rich stellar layers. This neutron-induced nucleosynthesis is likely connected to that of other isotopic signatures in presolar supernova grains. The Supplemental Material provides instructions that interested readers can follow for their own calculations of explosive nucleosynthesis and nuclear reaction rate sensitivities.

DOI: 10.1103/PhysRevC.89.025807 PACS number(s): 26.30.Ef, 25.30.Pt

I. INTRODUCTION

Presolar meteoritic grains are micron-sized or smaller dust grains whose origins predate the Sun. They are interstellar dust grains that were incorporated into primitive solid bodies in the forming Solar System. Collisions of these bodies release chunks, which fall to Earth as meteorites. The grains are recovered from the meteorites and analyzed isotopically, and their highly anomalous isotopic signatures show that they are condensates from outflows of stars (e.g., Ref. [1]) long dead by the time of condensation of the solar nebula.

Most presolar grains studied to date seem to have condensed in low-mass stellar outflows, but a significant fraction apparently formed in expanding and cooling ejecta from core-collapse supernovas. For example, most low-density graphites are probably supernova condensates [2], and a recent analysis of several such grains has shown spatially correlated hot spots of ^{15}N and ^{18}O within them [3]. This observation is of high significance because it points to the grains' origin. Figure 1 shows the presupernova and postsupernova mass fractions of ^{15}N and ^{18}O in the initially $15M_\odot$ stellar model s15a28 of Ref. [4] as a function of interior mass coordinate M_r. The interior mass is the mass contained inside a given (assumed spherical) shell in the star. It increases monotonically with stellar zone radius and is a useful coordinate for identifying a zone since the zone's radius increases or decreases during stellar evolution, but the interior mass remains fixed.

Large coexisting mass fractions of ^{15}N and ^{18}O occur in the helium-rich layer that stretches from interior mass coordinate $M_r \approx 3$–$3.8\ M_\odot$. This shell completed hydrogen burning and was in the process of burning helium to carbon and oxygen convectively when the star exploded and sent a shock through the outer layers, which compressed and heated them and then caused them to expand and cool and be injected into the interstellar medium. As evident from the figure, the ^{18}O is little affected by the stellar explosion—it is abundant in the helium shell by virtue of the partial burning of helium. The ^{15}N, on the other hand, shows a strong peak in the inner part of the helium shell that is entirely due to the explosive stellar nucleosynthesis. There is also an interesting supply of ^{15}N in the inner regions of the star ($M_r < 3\ M_\odot$), which is due to neutrino interactions. The large mass fractions of ^{15}N and ^{18}O in the inner helium-rich zones signal these regions as important source matter for the low-density graphite grains.

Because of the importance of ^{15}N as a diagnostic for unraveling the origin of supernova carbonaceous grains, we revisit the nucleosynthesis of ^{15}N in explosive burning in massive stars. We focus on explosive helium burning but also touch on ^{15}N explosive production in other parts of the star. There is a long and distinguished history to studies of explosive helium burning beginning with the pioneering work in the 1970s [5,6], and these works considered production of ^{15}N. In this work, we further delineate the nucleosynthesis pathways of ^{15}N in explosive helium burning and study the effects of reaction rate changes since the work of Ref. [4]. We emphasize the role of neutron-capture reactions, whose importance has perhaps not been fully recognized, and we link those reactions to production of other important cosmochemical signatures of explosive neutron-capture nucleosynthesis in helium-rich layers.

To carry out our studies, we develop a simple but realistic model of shock passage in a massive star. We apply this model to the particular presupernova stellar model s15a28. We implement our model with an open-source, freely available code project, and we provide detailed instructions in the accompanying Supplemental Material on how to download and compile the codes and run all of the calculations and create all of the figures presented in this paper [7]. Our hope is that interested readers will be able to use these instructions to run their own calculations of the explosive nucleosynthesis

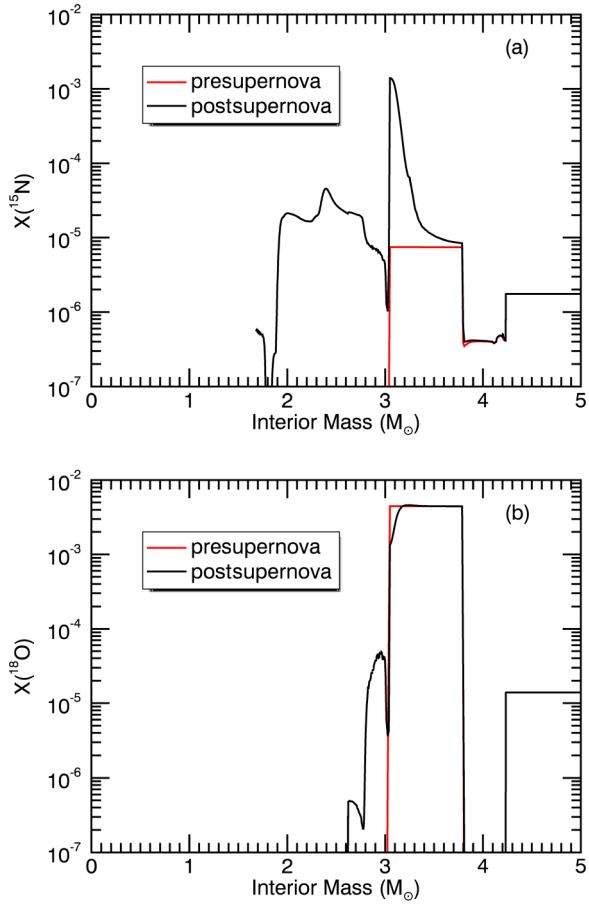

FIG. 1. (Color online) Presupernova and postsupernova mass fractions of (a) ^{15}N and (b) ^{18}O as a function of interior mass coordinate M_r for stellar model s15a28 of Ref. [4]. Only matter outside of $M_r = 1.68M_\odot$ is ejected; the remainder is left behind in the stellar remnant neutron star or black hole. The mass fractions of both species are also uniform in the envelope from $5M_\odot$ to the stellar surface, which was reduced by stellar winds during the star's lifetime from the initial $15M_\odot$ to $12.6M_\odot$ at the time of the explosion.

and reaction rate dependencies of other isotopes in s15a28 or other stellar models.

II. EXPLOSION MODEL

We seek a simple but realistic model of shock passage through the outer layers of a massive star. The shock generated by core collapse of the star travels outward and compresses, heats, and accelerates the initially unmoving (or slowly moving) stellar matter. Because of the large radial extent of most zones ejected in the explosion, we assume a planar geometry and neglect gravity. We also neglect viscosity, energy transfer, and relativistic effects during shock passage. In this case, in the frame of the shock, the Rankine-Hugoniot relations are

$$\rho_0 v_s = \rho v, \tag{1}$$

$$p_0 + \rho_0 v_s^2 = p + \rho v^2, \tag{2}$$

$$\rho_0 v_s \left(h_0 + \tfrac{1}{2} v_s^2\right) = \rho v \left(h + \tfrac{1}{2} v^2\right). \tag{3}$$

These equations express the conservation of mass, momentum, and energy across the shock, respectively. The quantities are ρ, the mass density, p, the pressure, and h, the specific enthalpy, which is given in terms of the specific internal energy e as

$$h = e + \frac{p}{\rho}. \tag{4}$$

The subscript 0 on a quantity indicates the quantity in the unshocked matter, while the quantity without a subscript is in the shocked matter. In the frame of the shock, the unshocked material is moving toward the shock with speed v_s, the shock speed in the star's frame. In the shock frame, the shocked material moves away from the shock with speed v. In the star's frame, the shocked matter moves in the same direction as the shock with speed $v_s - v$.

Substitution of Eq. (1) into Eq. (2) yields

$$v_s^2 = \frac{p_0}{\rho_0}\left(\frac{p}{p_0} - 1\right)\left(1 - \frac{\rho_0}{\rho}\right)^{-1}, \tag{5}$$

which gives the shock speed in terms of the pressures and densities. Substitution of Eqs. (1) and (2) into Eq. (3) gives

$$h - h_0 = \frac{1}{2}\left(\frac{1}{\rho_0} + \frac{1}{\rho}\right)(p - p_0). \tag{6}$$

The usefulness of Eq. (6) is that it relates quantities h and p, which are solely determined from the equation of state. The equation of state itself relates ρ, the temperature T, and the chemical composition. The quantities ρ_0 and T_0 and the chemical composition are known, so we can use the equation of state to compute h_0 and p_0. If T were known, we could then use the equation of state to solve Eq. (6) to find ρ, Eq. (5) to find v_s, and Eq. (1) to find v.

In general, however, we do not know T without solving the fluid dynamics equations for the problem at hand from our initial conditions. Our approach is instead to use the observation in Ref. [8] that the matter behind the supernova shock is well approximated as an isothermal ball because pressure waves in the postshock material tend to homogenize the energy density and the postshock energy density is dominated by the radiation. When the shock has reached radius r_s in the star, the energy behind the shock is thus given by

$$E = \tfrac{4}{3}\pi r_s^3 a T^4 \tag{7}$$

because the (assumed uniform) energy density is aT^4, where a is the radiation constant. By assuming an explosion energy E, we may then find the postshock temperature T and solve for the other postshock quantities, as described in the previous paragraph.

We implemented this procedure for solving for postshock conditions with the open-source NucNet Project *simple_snII* [9], which is built on top of NucNet Tools [10]. Figure 2 shows the temperature as a function of interior mass coordinate for several times in the explosion of the presupernova stellar model s15a28 of Ref. [4], as computed with *simple_snII* codes. The explosion energy for this calculation was $E = 1.0$ B (1 B = 1 bethe = 10^{51} ergs). At $t = 0$, the temperature structure of the star is that of the presupernova model. Zones inside of about $1.68M_\odot$ are not included in the

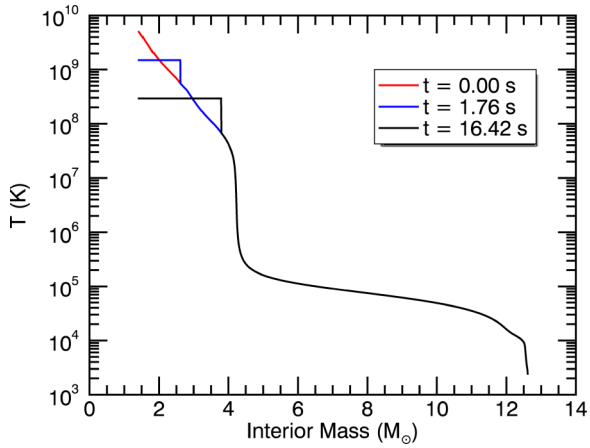

FIG. 2. (Color online) Temperature as a function of interior mass coordinate in the star during the $E = 1.0$ B explosion of s15a28. By construction, the material behind the shock has uniform temperature while the material outside of the shock's current position has its presupernova value.

stellar model output because they are taken to fall back into the stellar remnant. By $t = 1.76$ seconds, the shock has moved out to about $2.5M_\odot$. The temperature inside the shock is uniform (by construction of our model) and is just under 2×10^9 K. At $t = 16.42$ seconds, the shock has moved out to roughly $4M_\odot$, and the temperature of the isothermal shocked interior is about 3×10^8 K. As the radial coordinate r_s of the shock increases, the temperature declines, as evident from Eq. (7).

Figure 3 shows the time evolution of the temperature $T_9 = T/10^9$ K in zone 601 (at interior mass coordinate 3.05 $M_\odot$ and zone outer radial coordinate $r = 4.613 \times 10^9$ cm) in s15a28 for explosion energies 0.6 B and 1.0 B. Prior to shock passage, the zone is at its presupernova value (for zone 601, $T_9 = 0.241$). Because of the greater shock speed for greater explosion energy, a higher-energy shock will typically reach

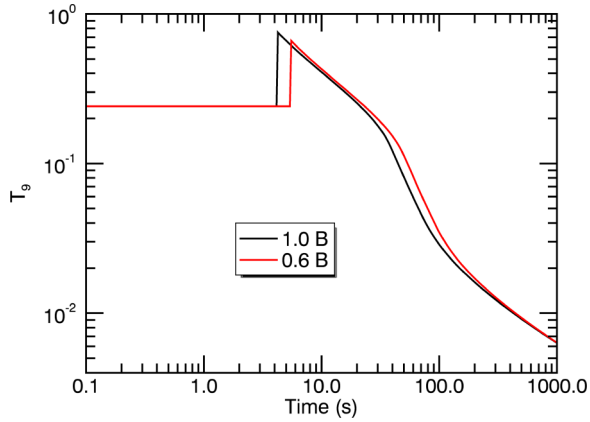

FIG. 3. (Color online) Temperature (in billions of Kelvins) as a function of time in zone 601 of s15a28 at interior mass coordinate $3.049M_\odot$ for explosion energies 0.6 B and 1.0 B. The lower-energy shock travels more slowly and therefore reaches zone 601 later than the higher-energy shock. The lower-energy shock also heats the zone to a lower peak temperature.

a given zone earlier than a lower-energy shock, as evident in Fig. 3. When the shock passes the zone, the temperature rises to a value given by Eq. (7), and the greater the energy, the higher the postshock temperature reached in our model. After the shock has passed, by our assumption of uniform temperature of the shocked material, the temperature of the zone is equal to the temperature of the zone that has just been shocked. This governs the subsequent temperature evolution of the zone. Since the postshock material is radiation-dominated, the density $\rho \propto T^3$.

Propagation of strong adiabatic blast waves in a medium with a power-law dependence of the density ρ_0 on radial coordinate r given by

$$\rho_0 = Ar^{-\omega} \tag{8}$$

is a self-similar problem [11,12]. The shock speed v_s may then be considered a function of the dimensionally independent quantities A (a constant), the explosion energy E, and the time t. From dimensional analysis, one may then find [12] that

$$v_s \propto [A^{-1}Et^{\omega-3}]^{\frac{1}{5-\omega}}. \tag{9}$$

From Eq. (9), we can easily understand the well-known result (cf. Ref. [11]) that, for $\omega < 5$, the shock accelerates if $\omega > 3$ and decelerates if $\omega < 3$. We may similarly find that the shock radius r_s behaves as

$$r_s \propto [A^{-1}Et^2]^{\frac{1}{5-\omega}}. \tag{10}$$

Figure 4 shows the shock speed as a function of M_r, as computed in our model from Eq. (5) as the shock crosses each zone in the star for explosion energy 1.0 B. It is clear that the shock's speed varies as the shock moves through the star. Figure 5 shows the quantity $\rho_0 r^n$ as a function of M_r in the presupernova star. Where the $n = 3$ curve is increasing with M_r (and r since r increases monotonically with M_r), $\omega < 3$. It is in these regions that the shock slows down as it moves through the star. In contrast, where the $n = 3$ curve has negative slope with M_r, the shock wave accelerates. The most notable feature of the shock speed is its dramatic rise above interior mass coordinate $4M_\odot$. This is where the density falls dramatically from the inner, denser regions of the star to

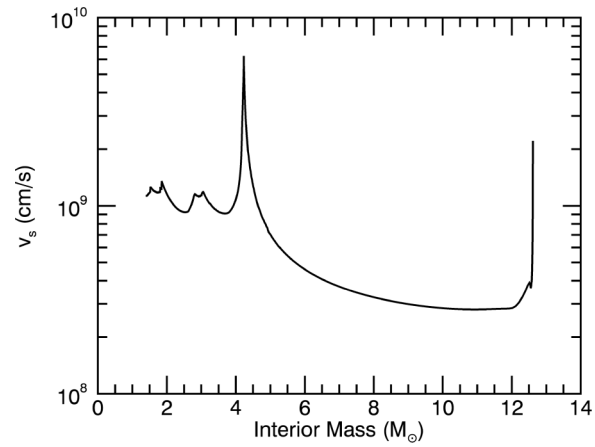

FIG. 4. Shock speed as a function of interior mass coordinate during the $E = 1.0$ B explosion of s15a28.

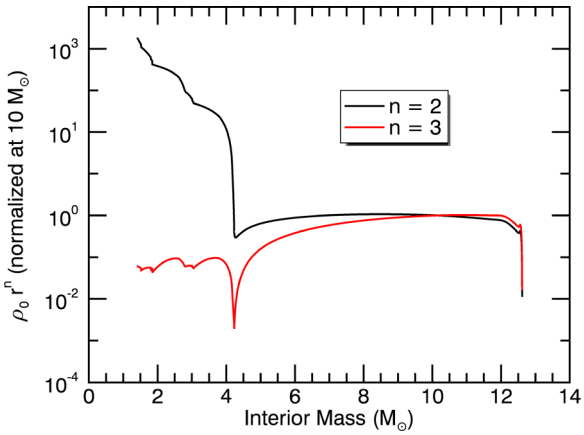

FIG. 5. (Color online) Run of the product of the density and the indicated power of the radial coordinate as a function of interior mass coordinate in s15a28. The curves have been normalized to unity at the interior mass coordinate of $10M_\odot$.

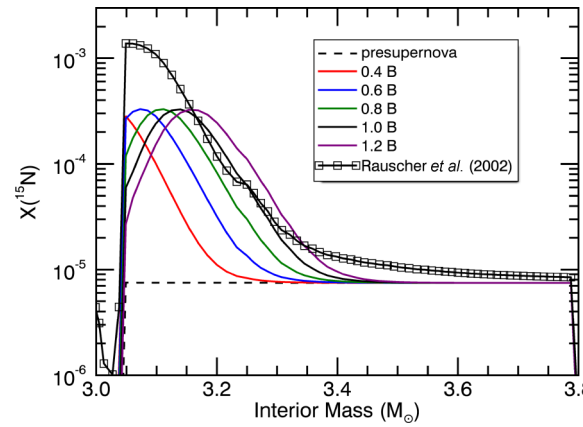

FIG. 6. (Color online) Final ^{15}N mass fraction as a function of interior mass coordinate 10^6 seconds after the explosion of s15a28 for the indicated explosion energies. Also shown for comparison are the presupernova and postsupernova values from Ref. [4].

the outer, tenuous envelope. Once the shock has run down this steep density gradient ($\omega > 3$), it reaches the shallower density run of the envelope and thus slows down. The correspondence between shock acceleration or deceleration and the behavior of the $\rho_0 r^3$ curve is less dramatic but clear in other places of the star as well.

From Eqs. (7) and (10), we may also note that

$$T \propto E^{\frac{1}{4}} r_s^{-\frac{3}{4}} \propto \left[A^{-\frac{3}{4}} E^{\frac{\omega-2}{4}} t^{\frac{3}{2}}\right]^{\frac{1}{\omega-5}}. \quad (11)$$

If $\omega = 2$, the evolution of T with time is independent of the explosion energy E. From Fig. 5, it is evident that in much of the envelope of the star, the density is well approximated as an $\omega = 2$ power law. This is why the two curves in Fig. 3 converge for times greater than several hundred seconds. For these late times, the shock has reached the envelope where ω is nearly 2 and the temperature-time relation is independent of E.

It is worth noting that, at a particular time t, a higher-energy shock has reached a larger radius than a lower-energy shock, which, by consideration of r_s alone in Eq. (7), suggests a lower temperature. On the other hand, at a particular r_s, the postshock temperature is higher for a higher-energy shock. This compensates the lower temperature expected for the larger r_s. When $\omega = 2$, these effects precisely balance out in our model and, at a particular time t, the higher- and lower-energy shocks result in the same postshock temperature even though the shocked volume is larger for the higher-energy shock.

III. NUCLEOSYNTHESIS

From thermodynamic trajectories derived from our explosion model, such as that shown in Fig. 3, we computed the resulting nucleosynthesis with our reaction network in Ref. [10]. We used the nuclear and reaction rate data in the REACLIBV2.0 snapshot from the JINA Reaclib database [13]. We ran the calculations over all 707 zones available in the presupernova star. These first calculations did not include the contribution of supernova neutrinos.

Figure 6 shows the ^{15}N mass fraction as a function of M_r in the helium zone for explosion energies 0.4 B, 0.6 B, 0.8 B, 1.0 B, and 1.2 B. The mass fractions are shown at 10^6 seconds after the explosion. Also shown are the presupernova and postsupernova values from Ref. [4]. Explosive nucleosynthesis caused by passage of the supernova shock has clearly increased the ^{15}N mass fraction, but not as much in our models as in Ref. [4]. We also note that for $E > 0.4$ B, the ^{15}N mass fraction first rises with increasing M_r, peaks, and then declines. The location of the peak increases in M_r with increasing explosion energy but the height is independent of E.

Figure 7 shows the integrated reaction currents in zone 608 at $M_r = 3.1395M_\odot$ for the $E = 1.0$ B explosion. Zone 608 contains the peak ^{15}N mass fraction for this explosion energy.

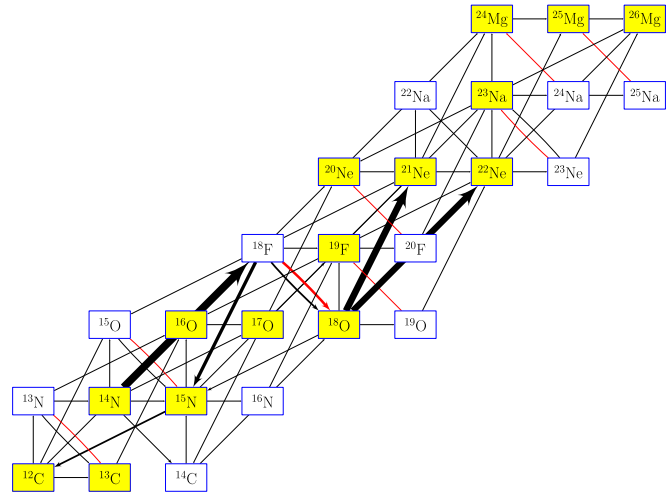

FIG. 7. (Color online) Integrated reaction currents in zone 608 (at $M_r = 3.1395M_\odot$) for the $E = 1.0$ B explosion of s15a28. In the print version of this figure, naturally occurring species are gray while in the online version they are yellow. In the print version, β decays are shown as dashed arrows while in the online version they are shown as red arrows.

We define the net current or flow $F[r](t)$ at a given instant in time t for a reaction r that links reactant j and product i as

$$F[r](t) = \left(\frac{dY_i}{dt}\right)_{r:j\to i} - \left(\frac{dY_i}{dt}\right)_{r:i\to j}, \qquad (12)$$

where $(dY_i/dt)_{r:j\to i}$ is the rate of increase of the abundance of species i due to reaction r while $(dY_i/dt)_{r:i\to j}$ is the rate of decrease of the abundance of i due to the same reaction. We then define the integrated current $I[r](t,t_0)$

$$I[r](t,t_0) = \int_{t_0}^{t} F[r](t')dt'. \qquad (13)$$

To construct the integrated currents graph, we compute $I[r](t,t_0)$ for each reaction. We then draw, for each reaction r, an arrow from each reactant j within the scope of the diagram to each product i with the thickness of the arrow proportional to the magnitude of the integrated current for that reaction. If the integrated current for reaction r is negative, the net flow for the reaction over the duration t_0 to t was in the reverse direction, so we reverse the direction of all arrows between reactants and products within the scope of the diagram for that reaction. Because of our linear scaling of the arrows with current magnitude, the sum of the thicknesses of the arrows going into a species minus the sum of the thicknesses of those leaving the species is proportional to the change in the species abundance from t_0 to t. In Fig. 7, we take $t_0 = 0$, the beginning of the explosion, and $t = 10^6$ seconds.

From Fig. 7, we see that the dominant production of ^{15}N over the course of the nucleosynthesis comes from the reaction sequence ^{14}N$(\alpha,\gamma)^{18}$F followed by ^{18}F$(n,\alpha)^{15}$N. The neutrons are primarily supplied by the reaction ^{18}O$(\alpha,n)^{21}$Ne. The reaction ^{18}O$(p,\alpha)^{15}$N also produces about 20% of the ^{15}N. The protons for this reaction are predominantly supplied by ^{18}F$(n,p)^{18}$O, although about 1/3 of the protons during the calculation come from ^{14}N$(n,p)^{14}$C. This means that the ^{18}F$(n,p)^{18}$O$(p,\alpha)^{15}$N channel is largely a self-proton-catalyzed version of the main ^{18}F$(n,\alpha)^{15}$N channel. Destruction of ^{15}N primarily occurs via ^{15}N$(p,\alpha)^{12}$C, although ^{15}N$(\alpha,\gamma)^{19}$F also contributes.

In the zones that will become part of the helium-burning shell at the time of the star's explosion, a large mass fraction of ^{14}N builds up during CNO cycling in presupernova core hydrogen burning. In the subsequent initial stages of helium burning, the reaction ^{14}N$(\alpha,\gamma)^{18}$F occurs but, due to the quiescent conditions, the neutron mass fraction is low, and the ^{18}F β decays to ^{18}O. This is the principal production mechanism for the abundant ^{18}O in the presupernova helium shell. It is in explosive burning that the ^{18}F can suffer a different fate.

Panel (a) of Fig. 8 shows the mass fractions of neutrons and protons during the calculation. Prior to shock passage, the density of zone 608 is 407.858 g/cc. The neutron abundance is $Y_n = 3.344 \times 10^{-19}$ per nucleon, so the neutron number density is $n_n = \rho N_A Y_n = 8.214 \times 10^7$ per cc (N_A is Avogadro's number), which is typical for helium-shell burning conditions. Following shock passage, the neutron density jumps to a peak value of 3.334×10^{17} per cc and then declines as the matter expands, which is high enough to allow for

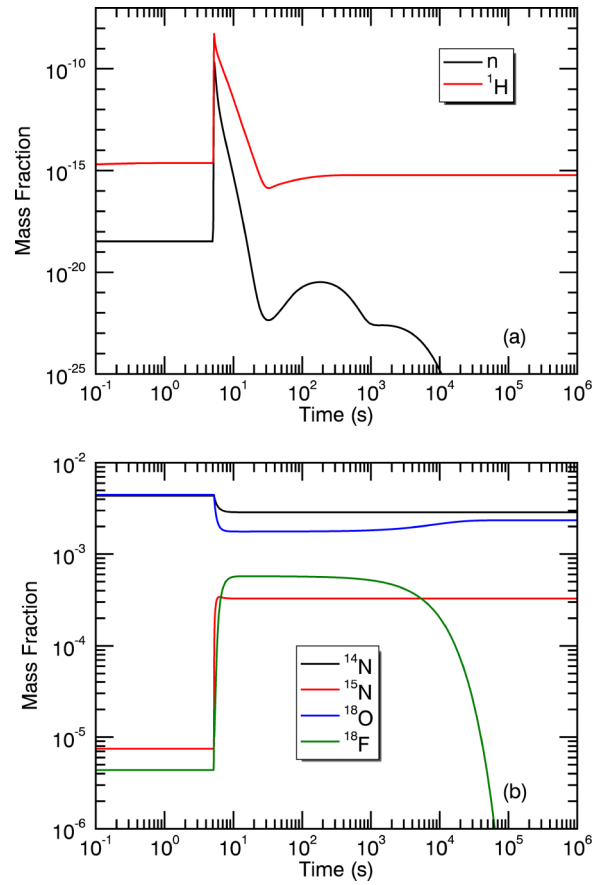

FIG. 8. (Color online) Time evolution of the mass fractions of (a) neutrons and protons and (b) other key species in zone 608 during the $E = 1.0$ B explosion of s15a28.

substantial destruction of ^{18}F by (n,α) and (n,p) reactions during the explosive burning.

About fifteen seconds after the explosion, the neutron mass fraction drops below its value prior to shock passage. It then rises to just above 10^{-21} before declining again. This late rise is due to β-delayed neutron emission by a small mass fraction of neutron-rich species created during the explosion by the burst of neutrons. For example, at $t = 152$ seconds, the dominant source of neutrons is the reaction $^{87}\mathrm{Br} \to {}^{86}\mathrm{Kr} + n + e^- + \bar{\nu}_e$. Interestingly, the dominant sink for the neutrons is still ^{18}F.

Panel (b) of Fig. 8 shows the mass fractions of ^{14}N, ^{15}N, ^{18}O, and ^{18}F during the calculation. The ^{14}N and ^{18}O mass fractions drop due to α capture while the ^{15}N and ^{18}F mass fractions rise. In the initial phases, any ^{18}F produced is quickly converted to ^{15}N by (n,α) or ^{18}O by (n,p), but, as the neutron mass fraction declines, this conversion slows, and the ^{18}F mass fraction eventually exceeds that of ^{15}N. Much later, the ^{18}F left over decays to ^{18}O. In fact, most of the initial ^{18}O present is destroyed during the nucleosynthesis and roughly 30% of the ^{18}O remaining at the end is newly produced via decay of the ^{18}F that did not convert to ^{15}N.

A species in the network reaches steady state when its rate of production equals its rate of destruction so that the rate of change of the abundance of the species goes to zero. From Fig. 7, we can consider production of ^{18}F predominantly to

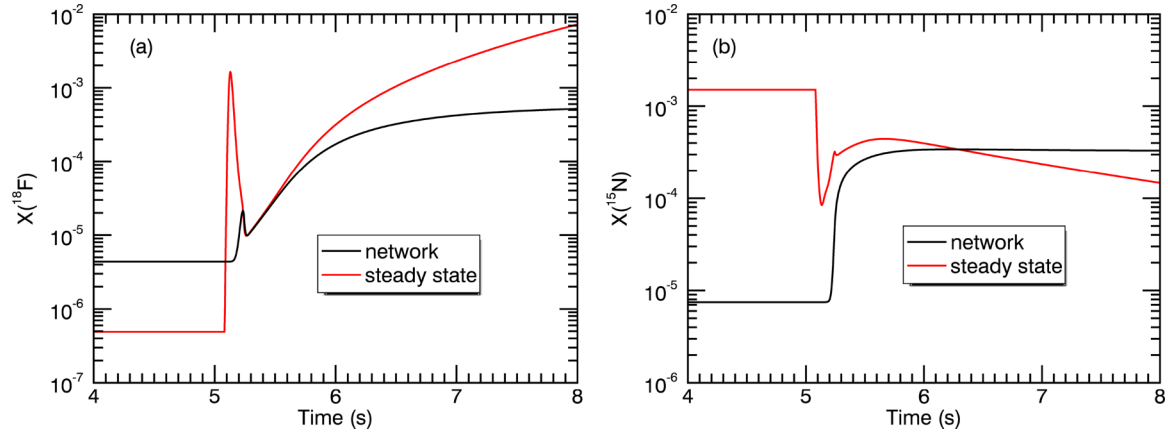

FIG. 9. (Color online) Time evolution of the mass fractions of (a) ^{18}F and (b) ^{15}N in zone 608 versus their steady-state values during the $E = 1.0$ B explosion of s15a28.

come from ^{14}N$(\alpha,\gamma)^{18}$F. The dominant destruction reactions are ^{18}F$(n,\alpha)^{15}$N and ^{18}F$(n,p)^{18}$O. If we limit our consideration to these production and destruction terms and assume that the ^{18}F abundance is in steady state, then

$$N_A\langle\sigma v\rangle_a \rho Y_{^{14}\mathrm{N}} Y_\alpha = N_A\langle\sigma v\rangle_b \rho \tilde{Y}_{^{18}\mathrm{F}} Y_n + N_A\langle\sigma v\rangle_c \rho \tilde{Y}_{^{18}\mathrm{F}} Y_n, \tag{14}$$

where $\tilde{Y}_{^{18}\mathrm{F}}$ denotes the steady-state abundance of ^{18}F and $\langle\sigma v\rangle$ is the thermally averaged product of the reaction cross section and reactant velocity. The subscripts a, b, and c respectively refer to the reactions ^{14}N$(\alpha,\gamma)^{18}$F, ^{18}F$(n,\alpha)^{15}$N, and ^{18}F$(n,p)^{18}$O. We may easily solve Eq. (14) for $\tilde{Y}_{^{18}\mathrm{F}}$:

$$\tilde{Y}_{^{18}\mathrm{F}} = \frac{\langle\sigma v\rangle_a Y_{^{14}\mathrm{N}} Y_\alpha}{(\langle\sigma v\rangle_b + \langle\sigma v\rangle_c) Y_n}. \tag{15}$$

The steady-state abundance of ^{18}F depends on the thermally averaged products of reaction cross section and reactant velocity and on the abundances of ^{14}N, α particles, and neutrons. These quantities change during the network calculation, but as long as the ^{18}F abundance changes rapidly enough, it can remain in steady state. A similar analysis can be made for other species once the dominant production and destruction reactions have been identified.

Figure 9 shows the mass fractions of ^{18}F and ^{15}N and their steady-state values in zone 608 during the $E = 1.0$ B explosion of s15a28. We note that the code to compute the steady-state abundances uses all production and destruction reactions for the species. Upon shock passage, the steady-state mass fraction of ^{18}F first spikes at 5.1 seconds. Initially, production dominates by ^{14}N$(\alpha,\gamma)^{18}$F, which increases the steady-state value. Once an abundance of neutrons builds up, however, the destruction of ^{18}F increases and the steady-state value drops by 5.3 seconds. Then, as the neutrons disappear and the destruction rate of ^{18}F falls, the steady-state value rises again.

The network ^{18}F mass fraction achieves steady state around 5.2 seconds and maintains it for several tenths of a second. Eventually, however, the production of ^{18}F declines as the capture of α particles by ^{14}N slows due to the falling temperature, and the network is not able to keep the ^{18}F mass fraction in steady state. The ^{15}N mass fraction never attains steady state. Nevertheless, most of the buildup of ^{15}N occurs while ^{18}F is in steady state.

Figure 10 shows the integrated current differences between zone 603 (at $M_r = 3.0728 M_\odot$) and zone 608 for the explosion with energy 1.0 B. To construct this graph, we computed the integrated currents in zone 603 and from those subtracted the currents in zone 608. Figure 10 then shows these current differences as arrows with the thickness of each arrow proportional to the current difference. In our model, zone 603 reaches a higher peak temperature (and density) than zone 608. As evident from Fig. 10, the largest current difference is for the reaction ^{18}O$(\alpha,n)^{21}$Ne, which results in a higher density of neutrons in zone 603 during the nucleosynthesis. Zone 603 also has a higher integrated current for the reaction ^{14}N$(\alpha,\gamma)^{18}$F, which, together with the increased neutron density, leads to larger production of ^{15}N in zone 603. However, there is also larger destruction of ^{15}N by ^{15}N$(p,\alpha)^{12}$C and ^{15}N$(\alpha,\gamma)^{19}$F.

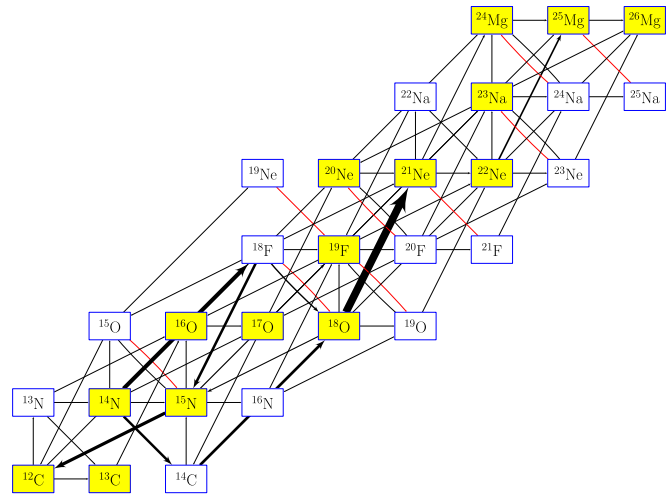

FIG. 10. (Color online) Integrated reaction current differences between zones 603 and 608 for the $E = 1.0$ B explosion of s15a28. See the caption to Fig. 7 for more information on the colors and arrow styles in the graph.

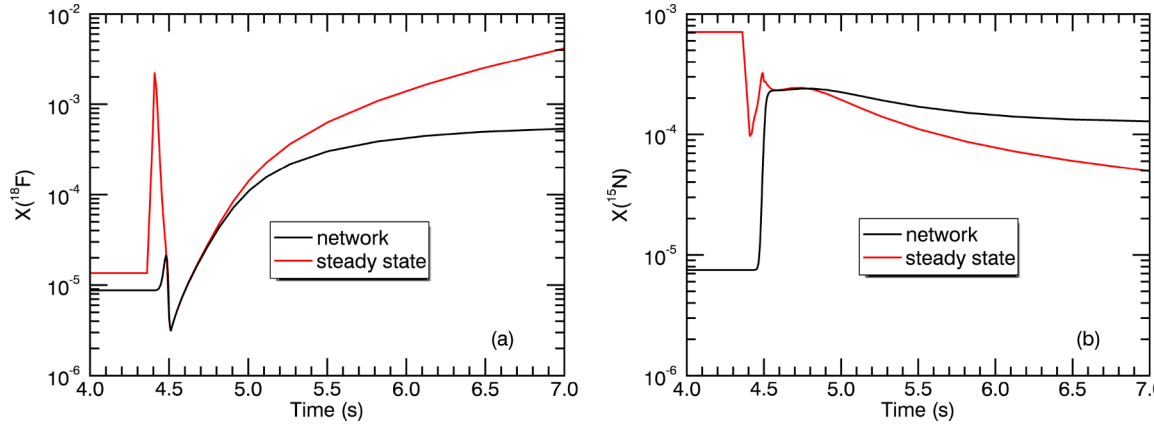

FIG. 11. (Color online) Time evolution of the mass fractions of (a) ^{18}F and (b) ^{15}N in zone 603 versus their steady-state values during the $E = 1.0$ B explosion of s15a28.

From the greater net thickness of arrows out of than into ^{15}N, we can infer that zone 603 produces less ^{15}N than zone 608. Quantitatively, the total integrated current difference between zones 603 and 608 for reactions producing ^{15}N is 6.9776×10^{-5} per nucleon and for reactions destroying ^{15}N is 8.3279×10^{-5} per nucleon, so the ^{15}N abundance is 1.3502×10^{-5} per nucleon less in zone 603 than in zone 608.

Figure 11 shows the network and steady-state mass fractions of ^{18}F and ^{15}N in zone 603 during the $E = 1.0$ B explosion of s15a28. The ^{18}F mass fraction is in steady state as the ^{15}N mass fraction builds up. This means that the increased postshock neutron mass fraction from the increased ^{18}O$(\alpha,n)^{21}$Ne flow does not itself result in a larger flow to ^{15}N. Production of ^{15}N is predominantly from ^{18}F$(n,\alpha)^{15}$N; thus, the rate of increase of the abundance of ^{15}N, here denoted $P_{^{15}\mathrm{N}}$, is

$$P_{^{15}\mathrm{N}} = N_A \langle \sigma v \rangle_b \rho Y_{^{18}\mathrm{F}} Y_n. \tag{16}$$

If the ^{18}F abundance is in steady state, we may use Eq. (15) to find

$$P_{^{15}\mathrm{N}} = \left(\frac{\langle \sigma v \rangle_b}{\langle \sigma v \rangle_b + \langle \sigma v \rangle_c} \right) N_A \langle \sigma v \rangle_a \rho Y_{^{14}\mathrm{N}} Y_\alpha. \tag{17}$$

[Recall that the subscripts a, b, and c respectively refer to the reactions ^{14}N$(\alpha,\gamma)^{18}$F, ^{18}F$(n,\alpha)^{15}$N, and ^{18}F$(n,p)^{18}$O.] Equation (17) shows that, when the ^{18}F abundance is in steady state, the reaction flow to ^{15}N from ^{14}N is independent of the neutron density. Of course, the higher neutron abundance means the steady-state abundance of ^{18}F will be lower [cf. Eq. (15)].

The zone 603 ^{15}N mass fraction does manage to attain an approximate steady state for a short time during the nucleosynthesis. This steady state occurs when the ^{15}N mass fraction reaches its maximum value. Due to the high destruction rates of ^{15}N at later times, the steady-state mass fraction declines, and the network attempts to keep pace. It is worth noting that the maximum postshock ^{15}N steady-state mass fraction for zone 603 is in fact less than that for zone 608; thus, the higher ^{15}N destruction rates for zone 603 result in a lower final ^{15}N mass fraction in zone 603 because the peak ^{15}N mass fraction reached is lower than in zone 608 and because the subsequent destruction is greater.

Figure 12 shows the integrated current differences between zone 613 (at $M_r = 3.2164 M_\odot$) and zone 608 for the explosion with energy 1.0 B. A number of the arrows in Fig. 7 are reversed in Fig. 12, which shows that these currents are less in zone 613 than in zone 608. This is expected since zone 613 reaches a lower peak temperature. Despite the reversal of the arrows, the net thickness of arrows leading out of ^{15}N is greater than the net thickness of arrows leading in, and the final abundance of ^{15}N in zone 613 is less than in zone 608. The total integrated current difference between zones 613 and 608 for reactions producing ^{15}N is -4.4845×10^{-5} per nucleon and for reactions destroying ^{15}N is -3.0719×10^{-5} per nucleon, so the ^{15}N abundance is 1.4126×10^{-5} per nucleon less in zone 613 than in zone 608.

Figure 13 shows the network and steady-state mass fractions of ^{18}F and ^{15}N in zone 613 during the $E = 1.0$ B explosion

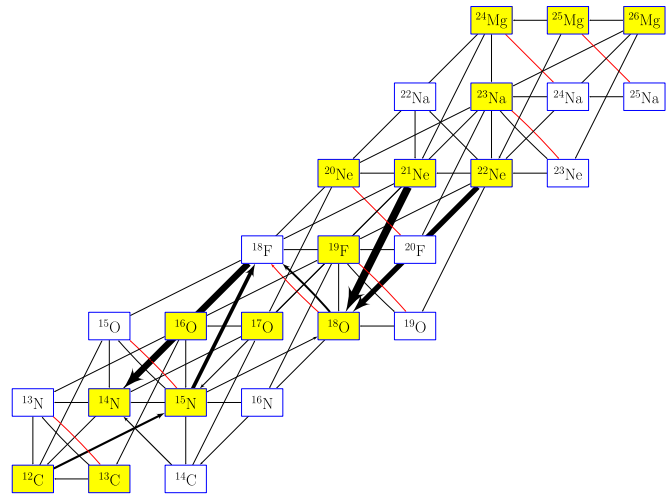

FIG. 12. (Color online) Integrated reaction current differences between zones 613 and 608 for the $E = 1.0$ B explosion of s15a28. See the caption to Fig. 7 for more information on the colors and arrow styles in the graph.

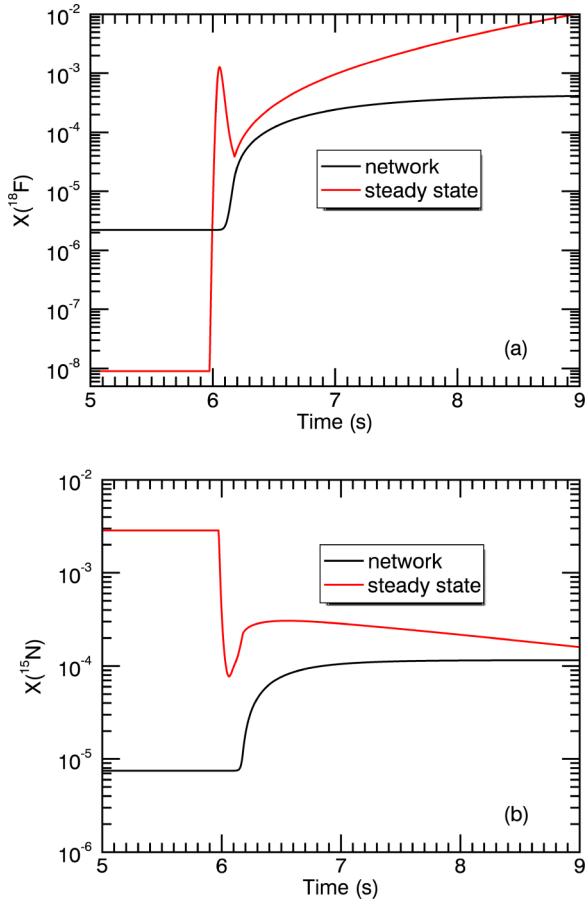

FIG. 13. (Color online) Time evolution of the mass fractions of (a) ^{18}F and (b) ^{15}N in zone 613 versus their steady-state values during the $E = 1.0$ B explosion of s15a28.

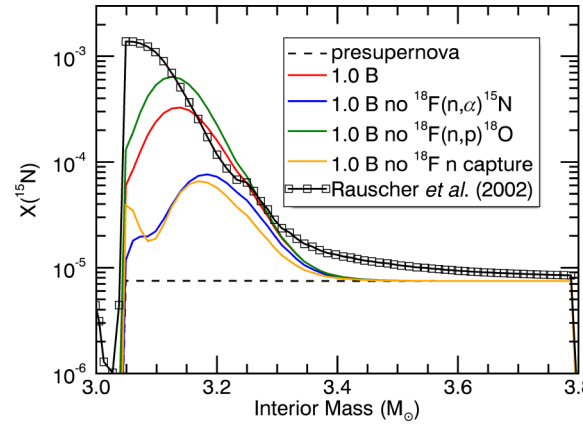

FIG. 14. (Color online) Final ^{15}N mass fraction as a function of interior mass coordinate 10^6 seconds after the explosion for the $E = 1.0$ B explosion of s15a28 when the ^{18}F$(n,\alpha)^{15}$N reaction was not included, the ^{18}F$(n,p)^{18}$O reaction was not included, and any ^{18}F neutron-capture reactions were not included. Also shown for comparison are the presupernova and postsupernova values from Ref. [4].

of s15a28. Neither species achieves steady state. The time scale for a species to attain steady state depends on the total destruction rate of the species. For this calculation of zone 613, the rate of change of the abundance of both ^{18}F and ^{15}N is always smaller than the rates at which the temperature and density are changing and so those species cannot reach steady state.

The reason for the peak in the ^{15}N mass fraction versus M_r in Fig. 6 is now clear. If the zone reaches too high a temperature, there is significant production of ^{15}N from ^{14}N and ^{18}O but greater destruction via proton and α capture than in the peak. If the zone reaches too low a temperature, there is less production of ^{15}N than in the peak. The peak is where ^{15}N production is optimal against destruction. Since the postshock temperature for a zone increases with increasing explosion energy, the ^{15}N peak moves out to larger M_r with increasing explosion energy E. The balance between ^{15}N production and destruction, however, keeps the ^{15}N mass fraction peak height nearly independent of E.

Our results show that, at least for the model under consideration, ^{18}F neutron capture plays a key role in explosive helium-burning synthesis of ^{15}N. Though modern calculations include these neutron-capture reactions, their role seems not to have been fully recognized. The pioneering survey of explosive nucleosynthesis in helium-rich layers by Howard, Arnett, and Clayton did not include ^{18}F neutron-capture or proton-capture reactions that would lead to ^{15}N or ^{15}O [5]. In that work, ^{15}N was produced predominantly as ^{15}O by ^{14}N$(p,\gamma)^{15}$O with a contribution from ^{18}O$(p,\alpha)^{15}$N. Later studies did include the relevant reactions and found that ^{18}F could play a dominant role, though it seems the focus for ^{15}N production was on ^{18}F$(p,\alpha)^{15}$O (e.g., Refs. [6,14]). It is likely those calculations did not achieve the high neutron densities that would allow the ^{18}F neutron-capture reactions to play a dominant role in ^{15}N synthesis. Explosion calculations of modern stellar models do allow for such high neutron densities.

We amplify this point in Fig. 14, which shows what happens when we do not include (1) the ^{18}F$(n,\alpha)^{15}$N reaction, (2) the ^{18}F$(n,p)^{18}$O reaction, and (3) any ^{18}F neutron-capture reactions. Without ^{18}F$(n,\alpha)^{15}$N, the peak ^{15}N mass fraction is a factor of $\sim$4 lower than with the reaction. The reason for this is in fact somewhat subtle. Figure 15 shows the integrated current differences for zone 608 in the $E = 1.0$ B explosion between the calculation without and with ^{18}F$(n,\alpha)^{15}$N. By shutting off ^{18}F$(n,\alpha)^{15}$N, the flow is almost entirely diverted to ^{18}F$(n,p)^{18}$O$(p,\alpha)^{15}$N, the self-proton-catalyzing route discussed above. We note, however, that the protons produced by ^{18}F$(n,p)^{18}$O are absorbed not only by ^{18}O, which increases ^{15}N, but also by ^{15}N, which decreases ^{15}N and limits the supply of protons for further capture on ^{18}O. The result is a much lower abundance of ^{15}N when the (n,α) reaction is disabled. Graphically, in Fig. 15, the thickness of the arrow from ^{18}F to ^{18}O is proportional to the increase in the total production of protons when we disable ^{18}F$(n,\alpha)^{15}$N, but, since the extra protons so produced during the calculation are essentially entirely consumed, that arrow thickness nearly equals the sum of the arrow thicknesses from ^{18}O to ^{15}N (which adds to the ^{15}N abundance) and from ^{15}N to ^{12}C (which subtracts from the ^{15}N abundance), the main proton sinks.

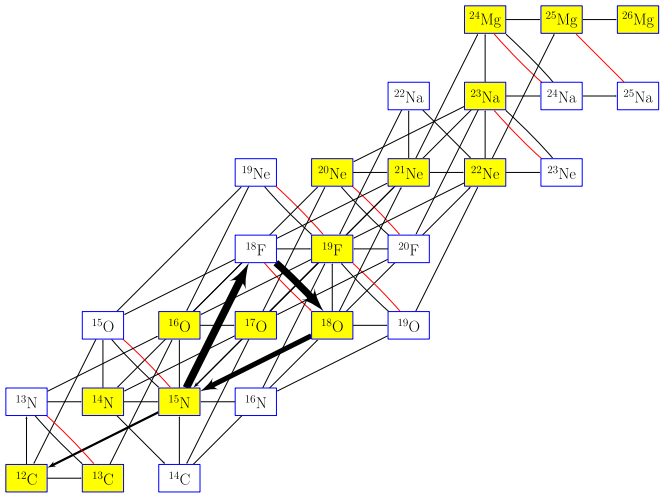

FIG. 15. (Color online) Integrated reaction current differences in zone 608 for the $E = 1.0$ B explosion of s15a28 between the calculation without and with the ^{18}F$(n,\alpha)^{15}$N reaction.

From these considerations we may see that, when the ^{18}F$(n,\alpha)^{15}$N reaction is active, the production of ^{15}N tends to work against ^{15}N destruction. Channeling more of the ^{18}F flow into (n,α) decreases production of protons by (n,p) and lowers the destruction of ^{15}N by ^{15}N$(p,\alpha)^{12}$C. Of course, the (n,α) reaction returns an α particle, which contributes to ^{15}N destruction by $^{15}N(\alpha,\gamma)^{19}$F, but these α particles are trivial in abundance compared to the α particles already present and the increased production from the (n,α) reaction is partially offset by the decreased production from (p,α) reactions. When the (n,p) reaction is entirely disabled, the resulting peak ^{15}N mass fraction is increased by a factor of $\sim$2 due to the lower (p,α) destruction.

Figure 14 also shows that disabling all ^{18}F neutron-capture reactions limits ^{15}N peak production even further, although there are zones away from the peak where the production is nearly as large as in the case with only the (n,α) reaction shut off. Disabling ^{18}F$(n,\alpha)^{15}$N leaves ^{18}O$(p,\alpha)^{15}$N as the only significant pathway for production of ^{15}N. Without ^{18}F$(n,p)^{18}$O available as a source of protons, however, the ^{18}O proton-capture flow decreases. The now-dominant production of protons occurs via ^{14}N$(n,p)^{14}$C, which has a much smaller cross section than ^{18}F$(n,p)^{18}$O in the temperature range of interest and thereby results in lower proton production during the nucleosynthesis and the aforementioned smaller ^{18}O$(p,\alpha)^{15}$N flow. Nevertheless, in some zones, the smaller proton fluence when all ^{18}F neutron-capture reactions are disabled gives the same production of ^{15}N as when ^{18}O$(p,\alpha)^{15}$N and ^{15}N$(p,\alpha)^{12}$C compete against each other in the absence of the (n,α) reaction alone.

IV. COMPARISON WITH RAUSCHER *ET AL.*

That the postexplosion helium-shell peak mass fraction of ^{15}N is nearly independent of the explosion energy E suggests the discrepancy between the level of ^{15}N production in our calculations and those of Ref. [4] is due to differences in reaction rates used in the calculations. To explore this possibility, we constructed a set (called "Set 2") of nineteen reactions possibly involved in the production or destruction of ^{15}N in explosive helium burning based on the reaction set used by Ref. [4]. Table I shows the nineteen reactions. The typically four-character code used to identify the reaction rate reference is that employed by the JINA database [13] or by Ref. [4]. The only discrepancy between this set and that of Ref. [4] is that the latter authors use Ref. [15] for ^{18}O$(\alpha,\gamma)^{22}$Ne while we use the rate expression in Ref. [16], which uses the resonance data in Ref. [15].

TABLE I. Rate sources: cf88 [38], dh03 [16], fcz2 [39], fkth [40,41], hfcz [42], il10 [43–46], ka02 [47] la90 [48], li10 [49], ra94 [50], rpsm [51], wag [52], wies (private communication to authors of Ref. [4]), wk82 [53].

Reaction	REACLIBV2.0	Set 2
^{1}H + ^{14}C → ^{15}N + γ	il10	cf88
^{1}H + ^{18}F → ^{4}He + ^{15}O	il10	wk82
^{1}H + ^{18}F → ^{19}Ne + γ	il10	wk82
^{1}H + ^{15}N → ^{4}He + ^{12}C	nacr	hfcz
^{1}H + ^{15}N → ^1n + ^{15}O	nacr	cf88
^{1}H + ^{15}N → ^{16}O + γ	li10	fcz2
^{1}H + ^{17}O → ^{18}F + γ	il10	la90
^{1}H + ^{18}O → ^{19}F + γ	il10	cf88
^{1}H + ^{18}O → ^{4}He + ^{15}N	il10	cf88
^{4}He + ^{14}C → ^{18}O + γ	il10	cf88
^{4}He + ^{14}N → ^{18}F + γ	il10	fcz2
^{4}He + ^{15}N → ^{19}F + γ	il10	cf88
^{4}He + ^{18}O → ^1n + ^{21}Ne	nacr	cf88
^{4}He + ^{18}O → ^{22}Ne + γ	il10	dh03
^1n + ^{17}F → ^{18}F + γ	rpsm	fkth
^1n + ^{18}F → ^{19}F + γ	rpsm	fkth
^1n + ^{18}F → ^{1}H + ^{18}O	wag	fkth
^1n + ^{15}N → ^{16}N + γ	ka02	wies
^1n + ^{18}O → ^{19}O + γ	ka02	ra94

Figure 16 shows the rate per interacting pair for four key reactions in the synthesis of ^{15}N in explosive helium burning. The peak postshock temperature reached in the inner part of the helium shell is typically in the range $T_9 \approx 0.4$–0.7. In this temperature range, the REACLIBV2.0 and Set 2 rates can differ by up to a factor of $\sim$10.

We computed the explosive nucleosynthesis with rates updated from Set 2. To do this, the network code read in the rates from REACLIBV2.0 and then overwrote the rates for reactions in Table I with those from Set 2. Figure 17 shows the presupernova and postsupernova ^{15}N mass fractions from Ref. [4] and the ^{15}N mass fraction at 10^6 seconds after the explosion of s15a28 for energy 0.6 B with REACLIBV2.0 rates and with rates updated from Set 2. Our calculation with Set 2 rates matches the peak postshock ^{15}N mass fraction of Ref. [4] well.

Figure 18 shows the integrated reaction currents for the calculation with REACLIBV2.0 rates in zone 601 at $M_r = 3.049 M_\odot$, which is the innermost zone in the helium shell

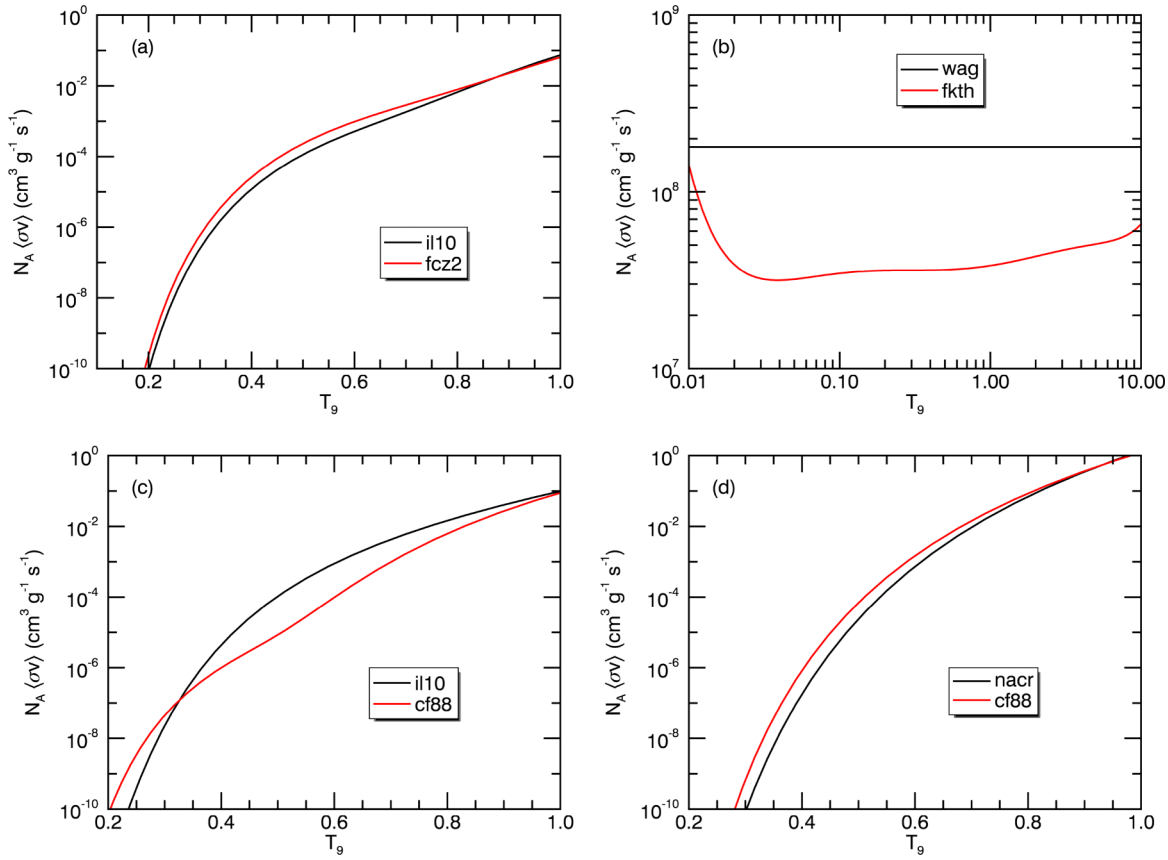

FIG. 16. (Color online) Reaction rates as a function of temperature (in billions of Kelvins). The reactions are (a) ^{14}N$(\alpha,\gamma)^{18}$F, (b) ^{18}F$(n,p)^{18}$O, (c) ^{15}N$(\alpha,\gamma)^{19}$F, and (d) ^{18}O$(\alpha,n)^{21}$Ne. The solid curves show rates from the REACLIBV2.0 snapshot. The dashed curves show rates from Set 2 (see Table I).

with abundant ^{14}N, for the $E = 0.6$ B explosion of s15a28. Figure 19 shows the integrated current differences between the $E = 0.6$ B calculation updated with Set 2 rates and the calculation with REACLIBV2.0 rates alone. By comparing these figures, we see that the calculation with rates updated from Set 2 has increased ^{15}N due to increased production and decreased

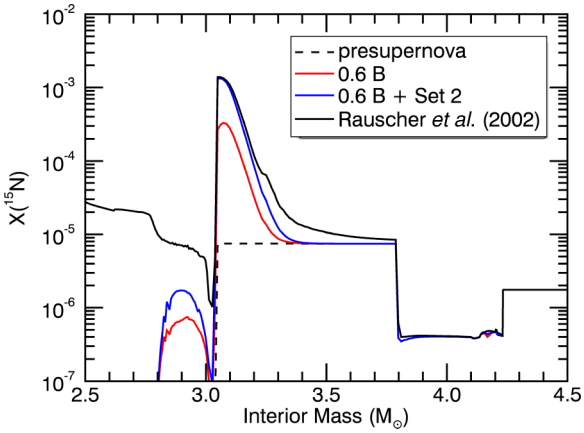

FIG. 17. (Color online) Final ^{15}N mass fraction as a function of interior mass coordinate 10^6 seconds after the explosion for the $E = 0.6$ B explosion of s15a28 with REACLIBV2.0 rates alone and with REACLIBV2.0 rates updated with Set 2 rates. Also shown for comparison are the presupernova and postsupernova values from Ref. [4].

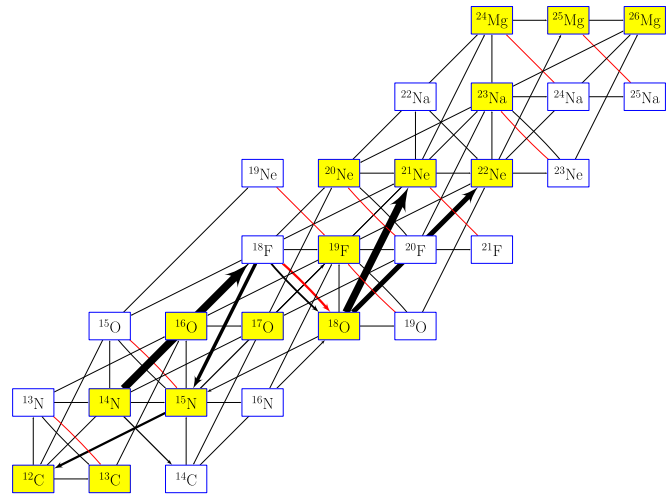

FIG. 18. (Color online) Integrated reaction currents in zone 601 (at $M_r = 3.049 M_\odot$) for the $E = 0.6$ B explosion of s15a28. See the caption to Fig. 7 for more information on the colors and arrow styles in the graph.

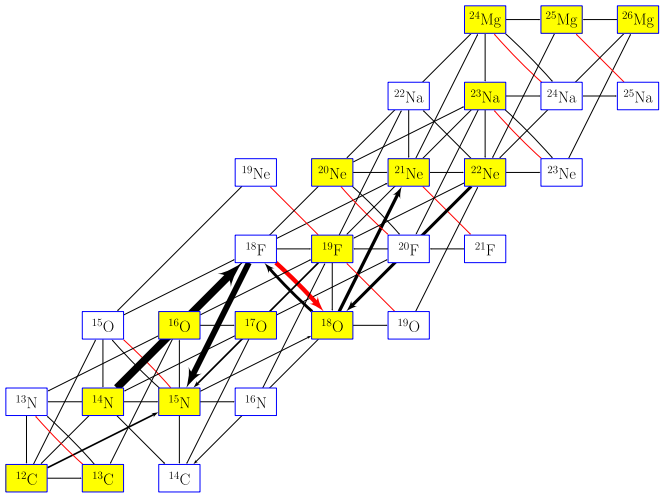

FIG. 19. (Color online) Integrated reaction current differences in zone 601 for the $E = 0.6$ B explosion of s15a28 between the calculation with and without rates updated from Set 2. See the caption to Fig. 7 for more information on the colors and arrow styles in the graph.

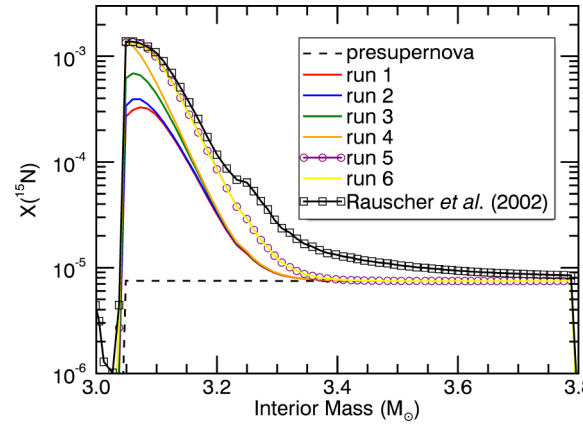

FIG. 20. (Color online) Final ^{15}N mass fraction as a function of interior mass coordinate 10^6 seconds after the explosion for the $E = 0.6$ B explosion of s15a28 for Runs 1–6. The curve for Run 6 lies on top of that for Run 5. For a description of the Runs, see the text. Also shown for comparison are the presupernova and postsupernova values from Ref. [4].

destruction. The increased production is from the enhanced ^{18}F$(n,\alpha)^{15}$N flow. This particular reaction is not in Set 2, but the increased current is due to enhanced production of ^{18}F from a faster ^{14}N$(\alpha,\gamma)^{18}$F reaction and greater production of neutrons by ^{18}O$(\alpha,n)^{21}$Ne, which increases in the Set 2 calculation at the expense of ^{18}O$(\alpha,\gamma)^{22}$Ne. There is less destruction of ^{15}N in the Set 2 calculation by either (α,γ) or (p,α). The only integrated reaction current that tends to decrease production of ^{15}N in the Set 2 calculation is ^{18}O$(p,\alpha)^{15}$N, but this decrease mostly comes from the lower production of ^{18}O by ^{18}F$(n,p)^{18}$O, which tends to maintain a higher abundance of ^{18}F and thereby increases the flow from that species to ^{15}N by (n,α).

To study the relative importance of the various reactions to the enhancement of ^{15}N in the Set 2 calculations, we ran four further calculations. We labeled the $E = 0.6$ B calculation with REACLIBV2.0 rates Run 1 and the $E = 0.6$ B calculation updated with Set 2 rates Run 6. Run 2 was Run 1 but with ^{14}N$(\alpha,\gamma)^{18}$F from Set 2. Run 3 was Run 2 but with ^{18}F$(n,p)^{18}$O from Set 2. Run 4 was Run 3 but with ^{15}N$(\alpha,\gamma)^{19}$F from Set 2. Run 5 was Run 4 but with ^{18}O$(\alpha,n)^{21}$Ne from Set 2. While the two reactions, ^{18}O$(p,\alpha)^{15}$N and ^{15}N$(p,\alpha)^{12}$C, play a role in ^{15}N synthesis, the differences between their rates in REACLIBV2.0 and Set 2 are less than a factor of two; thus, when we varied those rates between REACLIBV2.0 and Set 2, the resulting changes in the ^{15}N mass fraction were less than $\sim$3%, so we do not include them in these runs.

Figure 20 shows the results of Runs 1–6 for the postshock helium-zone ^{15}N mass fractions. All four reaction rates varied in Runs 2–5 play a role in the final ^{15}N mass fraction, especially in the inner part of the helium shell (near zone 601). The Set 2 ^{14}N$(\alpha,\gamma)^{18}$F rate is larger than that for REACLIBV2.0 in the relevant temperature range $T_9 \approx 0.4$–0.7. This increases the flow from ^{14}N to ^{18}F, which can then move to ^{15}N. The Set 2 ^{18}F$(n,p)^{18}$O rate is smaller than that for REACLIBV2.0. This partitions more of the neutron-capture flow to ^{15}N. The Set 2 ^{15}N$(\alpha,\gamma)^{19}$F rate is smaller than that for REACLIBV2.0, which decreases the destruction of ^{15}N. Finally, the Set 2 ^{18}O$(\alpha,n)^{21}$Ne rate is larger than that for REACLIBV2.0. This increases the neutron mass fraction immediately after shock passage and allows there to be more neutron capture from ^{18}F to ^{15}N. These rate variations account for almost all of the difference between the peak ^{15}N mass fraction in our $E = 0.6$ B calculation and that of Ref. [4].

We note that the higher Set 2 rate for ^{18}O$(\alpha,n)^{21}$Ne has little effect on the production of ^{15}N in the innermost part of the helium shell. Figure 21 shows that postshock production of ^{15}N during Run 4 occurs mostly while ^{18}F is in steady state. In this case, as Eq. (17) shows, the production of ^{15}N

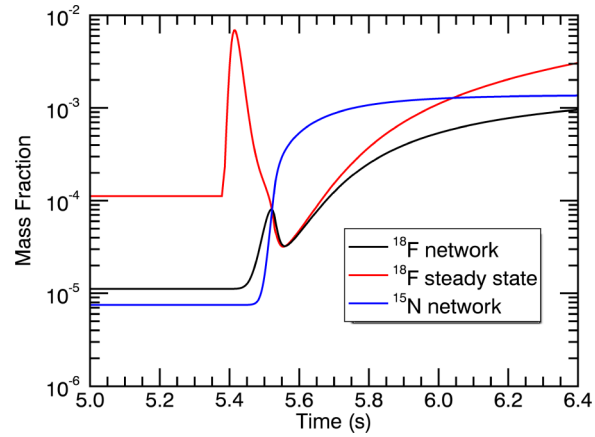

FIG. 21. (Color online) Time evolution of the mass fraction of ^{18}F in zone 601 versus its steady-state value during the Run 4 $E = 0.6$ B explosion of s15a28. Also shown is the mass fraction of ^{15}N as a function of time during the calculation. The buildup of the ^{15}N mass fraction largely occurs while the ^{18}F mass fraction is in an approximate steady state.

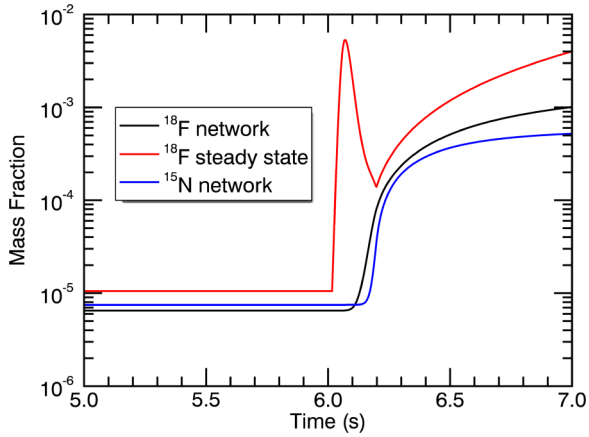

FIG. 22. (Color online) Time evolution of the mass fraction of ^{18}F in zone 605 versus its steady-state value during the Run 4 $E = 0.6$ B explosion of s15a28. Also shown is the mass fraction of ^{15}N as a function of time during the calculation. Unlike in zone 601 (cf. Fig. 21), the ^{18}F mass fraction is not in steady state when the ^{15}N mass fraction builds up.

is independent of the neutron abundance; thus, the increase in the neutron abundance from the enhanced ^{18}O$(\alpha,n)^{21}$Ne reaction rate has little effect on ^{15}N, although it decreases the steady-state abundance of ^{18}F.

At larger interior mass coordinates in the helium shell, the peak postshock neutron density is lower (due to lower peak temperature). In these outer layers, such as in zone 605 ($M_r = 3.098\ M_\odot$), ^{18}F does not attain steady state, as seen in Fig. 22. In this case, increasing the neutron density does enhance the net flow from ^{14}N to ^{15}N via ^{18}F and thereby increases the final ^{15}N mass fraction.

Figure 20 shows that a decrease in the rate for ^{18}F$(n,p)^{18}$O does increase the final mass fraction of ^{15}N in the innermost helium-shell zones even though the ^{18}F mass fraction during Run 2 is in steady state while the ^{15}N mass fraction grows after shock passage. Because of the steady state, the total neutron-capture flow out of ^{18}F does not change with this decrease in the (n,p) rate; rather, as apparent from Eq. (17), the decrease in the (n,p) rate apportions more of the flow into the (n,α) channel, which leads to ^{15}N. This means that any experimental reevaluation of ^{18}F neutron capture for the purpose of quantifying explosive helium-burning production of ^{15}N should focus on a consistent description of the competition among the relevant exit channels for ^{18}F neutron capture.

V. NEUTRINOS

Cooling of the nascent neutron star produced by stellar core collapse predominantly occurs via emission of neutrinos, and the calculations of Ref. [4] included the effects of interactions of these neutrinos with nuclei in the outer stellar layers. It is common to consider the neutrino luminosity L_ν to decay exponentially with time such that

$$L_\nu(t) = L_{\nu 0} \exp\{-t/\tau\}, \tag{18}$$

where $L_{\nu 0}$ is the initial neutrino luminosity and τ is an e-folding decay time. It is also common to consider the neutrino energy spectrum to be that of a black body at temperature T_ν; thus, the average neutrino energy is $\langle E_\nu \rangle = 3.15 T_\nu$, where T_ν is measured in units of energy. Under the assumption that neutrinos are streaming radially outward from the stellar core, we may thus find that the number flux $F_\nu(r,t)$ of neutrinos at radius r and time t is

$$F_\nu(r,t) = \frac{L_\nu(t)}{4\pi r^2 \langle E_\nu \rangle}. \tag{19}$$

Given a neutrino-nucleus interaction cross section σ_i for species i, the interaction rate is then $F_\nu(r,t)\sigma_i$.

The neutrinos come in three flavors, e, μ, and τ, and for each flavor x there is the neutrino ν_x and its antineutrino $\bar{\nu}_x$. We follow Ref. [4] and consider $T_\nu = 4$ MeV for ν_e and $\bar{\nu}_e$ and $T_\nu = 6$ MeV for the other four neutrino types. We partition 3×10^{53} ergs $= 300$ B amongst all six neutrinos; thus, $L_{\nu 0}\tau = 5 \times 10^{52}$ ergs for each neutrino. We took $\tau = 3$ seconds. For neutrino-nucleus interaction cross sections, we used neutrino-capture cross sections on free neutrons and protons from Ref. [17], neutrino-spallation cross sections on ^{4}He from Ref. [14], and all other neutrino-nucleus cross sections from Ref. [18].

The passing shock accelerates a parcel of matter. This is important for including neutrino interactions because, as Eq. (19) shows, the neutrino flux at a zone depends on the zone's radial coordinate $r(t)$. In our simple model, we take $r(t)$ of a zone to behave as

$$r(t) = \begin{cases} r_0 & \text{if} \quad t \leqslant t_s \\ r_0 + \alpha(v_s - v)(t - t_s) & \text{if} \quad t > t_s, \end{cases} \tag{20}$$

where r_0 is the initial radial coordinate for the zone, t_s is the time of shock passage, $v_s - v$ is the zone's postshock velocity in the star's frame, and α is a factor to scale the velocity. The quantity α allows us to model crudely the fluid interaction of a zone with the underlying and overlying material.

Figure 23 shows the final ^{15}N mass fraction we obtain for our $E = 0.6$ B explosion of s15a28 using the updated rates with and without neutrinos along with the presupernova mass fraction and explosive yield from Ref. [4]. Inclusion of neutrinos provides a much better agreement between our calculation and that of Ref. [4] in the outer part of the helium shell from $M_r \approx 3.3 - 3.8\ M_\odot$ and for $M_r < 3\ M_\odot$.

Figure 24 is identical to Fig. 23 except that it is for an explosion energy 1.0 B and we doubled the neutron and proton neutrino-spallation cross sections on ^{16}O and we also included a run with $\alpha = 0.2$ to see the effect of slowing down the postshock velocity [see Eq. (20)]. As recognized by the authors of Ref. [14], and as we explore further in Sec. V B, these cross sections play a role in synthesizing ^{15}N in the C/O-rich layers of the exploding star. The authors of Ref. [14] do not provide branching ratios for neutral-current interaction cross sections at $T_\nu = 6$ MeV. They do provide such data for $T_\nu = 8$ MeV, however, and we use that to compare our rates with those employed by Ref. [4], who used the Ref. [14] cross sections. From the data in Tables I and III of Ref. [14], we find at $T_\nu = 8$ MeV for ^{16}O a neutron neutrino-spallation cross section of 7.47×10^{-43} cm^2 and a proton neutrino-spallation cross

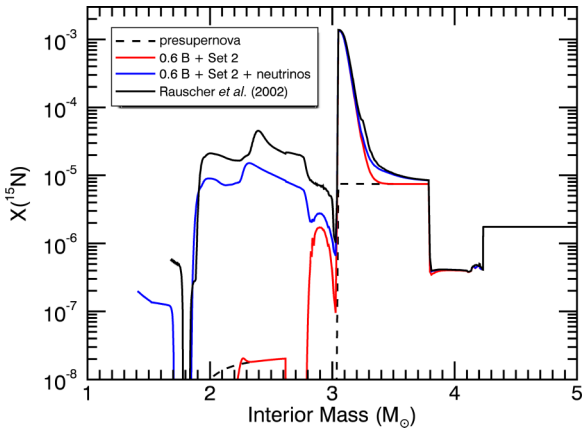

FIG. 23. (Color online) Final ^{15}N mass fraction as a function of interior mass coordinate 10^6 seconds after the explosion for the $E = 0.6$ B explosion of s15a28 with REACLIBV2.0 rates updated from Set 2 and with and without neutrino-nucleus interactions. Also shown for comparison are the presupernova and postsupernova values from Ref. [4].

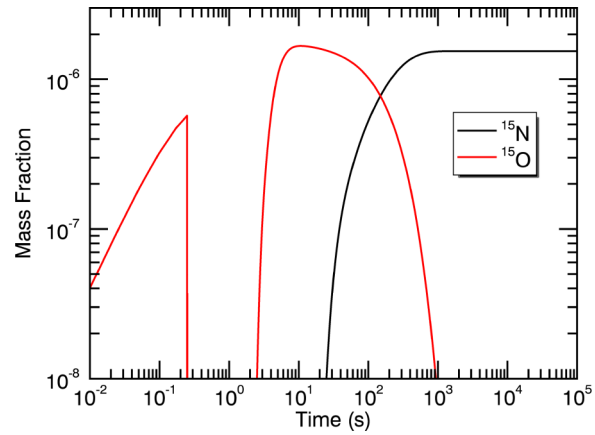

FIG. 25. (Color online) Time evolution of the mass fractions of ^{15}N and ^{15}O in zone 345 (at $M_r = 1.703 M_\odot$) during the $E = 1.0$ B explosion of s15a28. The calculation included the effects of neutrino-nucleus interactions and the nucleon neutrino-spallation cross sections on ^{16}O were doubled from our standard value in Ref. [18].

section of 2.68×10^{-42} cm^2. From the data in Ref. [18], we find the corresponding cross sections to be 3.05×10^{-43} cm^2 and 5.06×10^{-43} cm^2. A factor of two boost of our ^{16}O neutron and proton neutrino-spallation cross sections is thus reasonable to try to match the results of Ref. [4] better.

The overall fit of our result for ^{15}N to that of Ref. [4] in Fig. 24 is reasonable and the $\alpha = 0.2$ calculation is good to within about a factor of three. In the following, we use the $\alpha = 0.2$ calculation to study in detail how neutrino-nucleus interactions boost ^{15}N production in three particular zones.

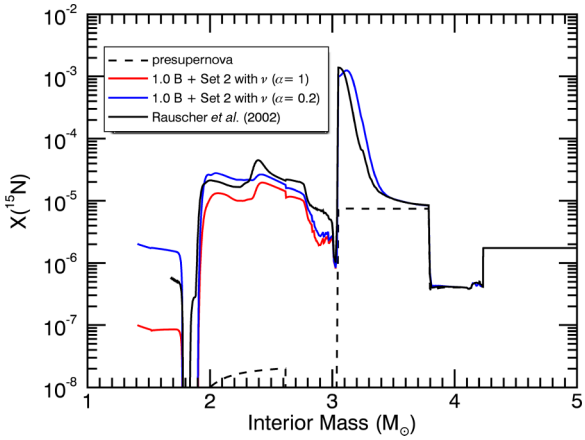

FIG. 24. (Color online) Final ^{15}N mass fraction as a function of interior mass coordinate 10^6 seconds after the explosion for the $E = 1.0$ B explosion of s15a28 with REACLIBV2.0 rates updated from Set 2 and with and without neutrino-nucleus interactions. In the calculations with neutrinos, we doubled the neutron and proton neutrino-spallation cross sections on ^{16}O from our standard value in Ref. [18] and we applied $\alpha = 1$ and $\alpha = 0.2$ [see Eq. (20)] to the runs. Also shown for comparison are the presupernova and postsupernova values from Ref. [4].

A. Zone 345

Figure 25 shows the ^{15}N and ^{15}O mass fractions in zone 345 (at $M_r = 1.703\ M_\odot$) during the $E = 1.0$ B explosion of s15a28. Early in the calculation, ^{15}O builds up. It is then destroyed when the matter heats up suddenly due to shock passage near $t = 0.25$ seconds. It builds up again for $t > 2$ seconds and eventually decays to ^{15}N.

Figure 26 shows the net reaction flows at $t = 0.0036$ seconds, which is before shock passage. To construct this figure, we compute all net reaction flows $F[r](t)$ from Eq. (12). We then draw, for each reaction r, an arrow from each reactant j within the scope of the diagram to each product i with the thickness of the arrow proportional to the magnitude of the net flow for that reaction. The initial buildup of ^{15}O occurs by the neutrino-spallation reaction $\nu_x + {}^{16}\mathrm{O} \rightarrow \nu_x' + {}^{15}\mathrm{O} + n$. In this case, ν_x represents the μ and τ neutrinos and their antineutrinos, which is why there are four neutrino reaction arrows from ^{16}O to ^{15}O. Neutrino-spallation production of ^{15}N is also occurring, but that ^{15}N is quickly destroyed by $^{15}\mathrm{N}(p,\alpha)^{12}\mathrm{C}$, so its abundance remains low. The protons for this reaction come from neutrino-spallation reactions on heavy species such as $\nu_x + {}^{28}\mathrm{Si} \rightarrow \nu_x' + {}^{27}\mathrm{Al} + p$ and $\nu_x + {}^{32}\mathrm{S} \rightarrow \nu_x' + {}^{31}\mathrm{P} + p$.

Upon shock passage, the matter in zone 345 compresses and heats up and then expands and cools. The matter undergoes an α-rich freeze out from equilibrium (e.g., Ref. [19]) in which much of the initially abundant silicon and sulfur break down into light nuclei (including α particles) and then reassemble to form ^{56}Ni, which has a final mass fraction of 0.835 before decay to ^{56}Co and, ultimately, ^{56}Fe. The final ^{4}He mass fraction is 0.035.

Figure 27 shows the net reaction flows at $t = 4.771$ seconds, a time when the ^{15}O is building back up after shock passage. The reaction sequence that produces most of the ^{15}O is $^7\mathrm{Be}(\alpha,\gamma)^{11}\mathrm{C}(\alpha,p)^{14}\mathrm{N}(p,\gamma)^{15}\mathrm{O}$. The authors of Ref. [14] recognized this reaction sequence up to ^{11}C as an interesting

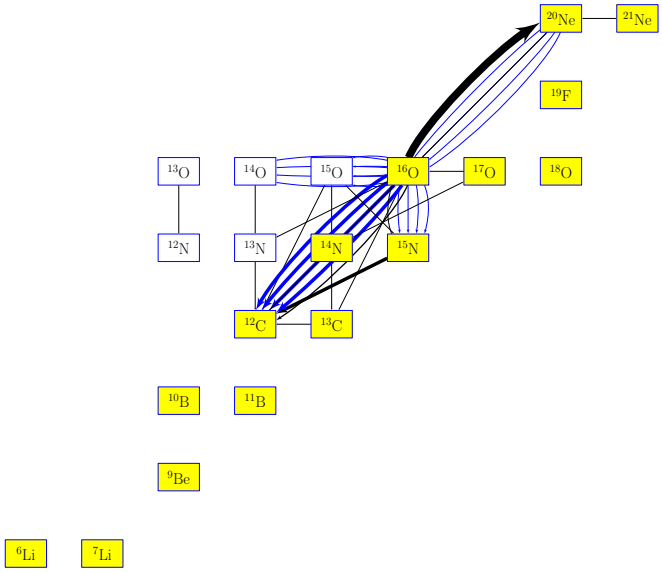

FIG. 26. (Color online) Net reaction flows for the calculation in Fig. 25 at $t = 0.0036$ seconds and $T_9 = 2.733$. In the print version of this figure, naturally occurring species are gray and dashed arrows represent neutrino-nucleus reactions while solid arrows represent all other reactions. In the online version, naturally occurring species are yellow and blue arrows represent neutrino-nucleus reactions while black arrows represent all other reactions. The maximum flow in the figure is 1.063×10^{-6} per nucleon per second.

source of ^{11}B. The ^{7}Be itself is produced by the reaction $^{3}\mathrm{He} + {}^{4}\mathrm{He} \rightarrow {}^{7}\mathrm{Be} + \gamma$, and the ^{3}He comes from neutrino spallation on ^{4}He: $\nu_x + {}^{4}\mathrm{He} \rightarrow \nu'_x + {}^{3}\mathrm{He} + n$.

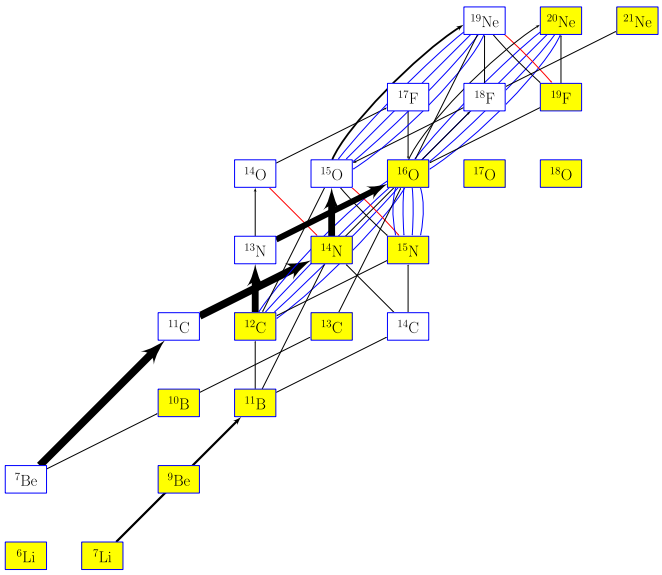

FIG. 27. (Color online) Net reaction flows for the calculation in Fig. 25 at $t = 4.771$ seconds and $T_9 = 0.6884$. See the caption to Fig. 26 for more information on the colors and arrow styles in the graph. The maximum flow in the figure is 4.093×10^{-8} per nucleon per second.

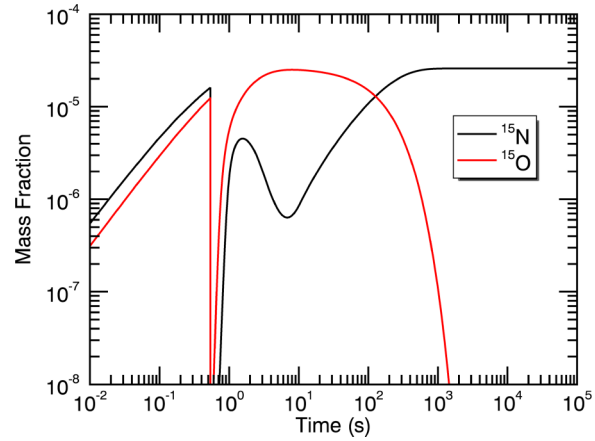

FIG. 28. (Color online) Time evolution of the mass fractions of ^{15}N and ^{15}O in zone 405 (at $M_r = 2.005 M_\odot$) during the $E = 1.0$ B explosion of s15a28. The calculation included the effects of neutrino-nucleus interactions and the nucleon neutrino-spallation cross sections on ^{16}O were doubled from our standard value in Ref. [18].

Clearly, abundant ^{4}He is necessary for this production sequence of ^{15}O (and, hence, ^{15}N). At slightly larger interior mass coordinate from zone 345, the freeze out becomes α poor. The low abundance of ^{4}He means that there is little production of ^{15}O by the above reaction sequence, which explains the sudden drop in the ^{15}N mass fraction near $M_r = 1.8\ M_\odot$. Also, as Fig. 24 shows, slowing the postshock outward movement of the material increases the neutrino fluence in the matter and, in turn, the interaction rate of neutrinos and α's and the resulting ^{15}N mass fraction in the nucleosynthesis.

B. Zone 405

Zone 405 (at $M_r = 2.005 M_\odot$) experienced presupernova carbon burning and is thus rich in ^{16}O, ^{20}Ne, and ^{24}Mg prior to shock passage. For the $E = 1.0$ B explosion, the zone reaches a peak postshock temperature $T_9 = 3.28$ and undergoes explosive neon burning in which the mass fraction of ^{16}O increases from 0.69 to 0.77.

Figure 28 shows the mass fractions of ^{15}N and ^{15}O in zone 405 during the $E = 1.0$ B explosion of s15a28. Before shock passage, both ^{15}N and ^{15}O build up by neutrino spallation on the abundant ^{16}O. Unlike in zone 345, the proton mass fraction remains low, so the ^{15}N thus produced is not destroyed. Upon shock passage, both species are destroyed but build up again once the temperature and density fall.

Figure 29 shows the net reaction flows at $t = 0.8665$ seconds. Again, neutrino-spallation reactions on ^{16}O produce both ^{15}O and ^{15}N. The growth of ^{15}N lags behind that of ^{15}O because of the destruction of ^{15}N by the (p,α) reaction. By $t \approx 1.5$ seconds, the neutrino flux has dropped significantly (both because of the declining neutrino luminosity and the outward movement of the zone) so that destruction of ^{15}N by (p,α) outstrips production by neutrinos, and the ^{15}N mass fraction declines. At $t \approx 10$ seconds, β decay of ^{15}O becomes the dominant source of ^{15}N, and the ^{15}N grows until the supply of parent ^{15}O is exhausted.

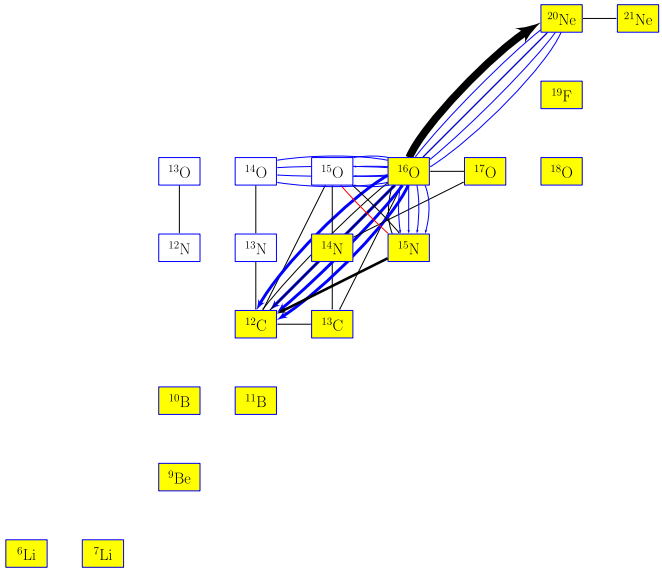

FIG. 29. (Color online) Net reaction flows for the calculation in Fig. 28 at $t = 0.8665$ seconds and $T_9 = 2.383$. See the caption to Fig. 26 for more information on the colors and arrow styles in the graph. The maximum flow in the figure is 6.86×10^{-6} per nucleon per second.

C. Zone 645

Zone 645 (at $M_r = 3.612 M_\odot$) is in the outer layers of the helium shell. As Fig. 6 shows, explosive helium burning does not modify the ^{15}N mass fraction in this zone for any of the explosion energies we have considered. If we include the effects of neutrinos, however, we do find an explosive ^{15}N yield in this zone that agrees well with that of Ref. [4].

Panel (a) of Fig. 30 shows the mass fractions of neutrons and protons in zone 645 during the $E = 1.0$ B explosion of s15a28. Prior to shock passage, the proton mass fraction builds up. This is due primarily to neutrino-spallation reactions on ^{4}He. The reaction $\nu_x + {}^4\mathrm{He} \rightarrow \nu_x' + {}^3\mathrm{H} + p$ directly produces protons. The proton mass fraction grows linearly with time early but starts to level off at $t \approx 1$ second as the neutrino flux declines. Protons are also produced from neutrons. The reaction $\nu_x + {}^4\mathrm{He} \rightarrow \nu_x' + {}^3\mathrm{He} + n$ produces neutrons, which are then converted to protons by (n,p) reactions such as $^{14}\mathrm{N}(n,p)^{14}\mathrm{C}$. These reactions come into balance quickly and the neutron mass fraction reaches a steady state. The neutron mass fraction declines after $t \approx 1$ second as the neutrino flux falls, briefly spikes as the shock passes and liberates neutrons by (p,n) and (α,n) reactions, and then drops again as the matter expands and cools.

When the shock passes, the protons created by the preshock neutrino-spallation reactions are quickly consumed. The dominant sink for the protons is $^{18}\mathrm{O}(p,\alpha)^{15}\mathrm{N}$, which enhances the ^{15}N mass fraction. At the time of shock passage, the proton abundance is 9.91×10^{-8} per nucleon. During the explosive burning, an additional proton abundance of 2.83×10^{-8} per nucleon is generated, giving a total proton abundance of 1.27×10^{-7} per nucleon generated during the calculation. The ^{15}N abundance changes from its initial value

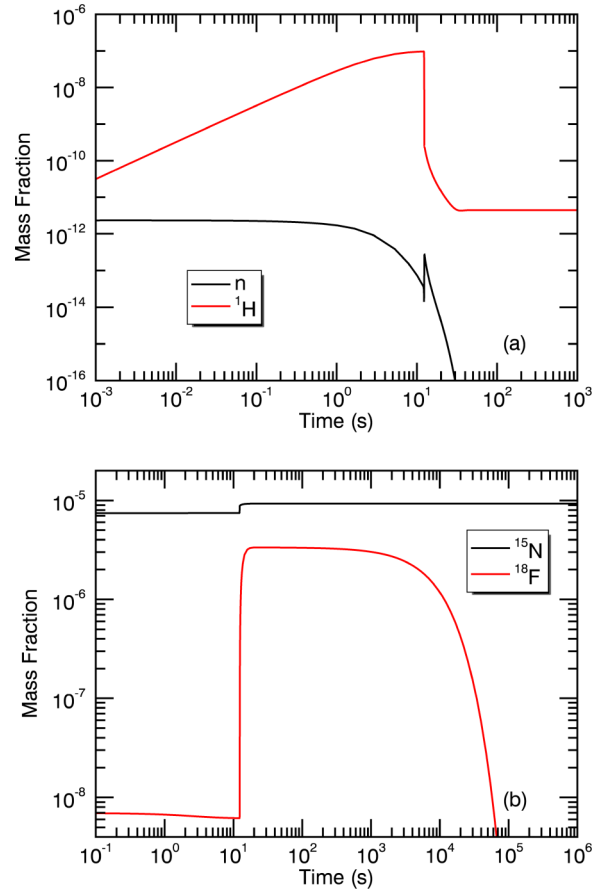

FIG. 30. (Color online) Time evolution of the mass fractions of (a) neutrons and protons and (b) ^{15}N and ^{18}F in zone 645 (at $M_r = 3.612 M_\odot$) during the $E = 1.0$ B explosion of s15a28. The calculation included the effects of neutrino-nucleus interactions and the nucleon neutrino-spallation cross sections on ^{16}O were doubled from our standard value in Ref. [18].

of $7.46 \times 10^{-6}/15 = 4.97 \times 10^{-7}$ per nucleon to a final value of $9.33 \times 10^{-6}/15 = 6.22 \times 10^{-7}$ per nucleon, corresponding to an abundance increase of 1.25×10^{-7} per nucleon. The integrated current of $^{18}\mathrm{O}(p,\alpha)^{15}\mathrm{N}$ is 1.22×10^{-7} per nucleon, thus accounting for almost the entire increase in ^{15}N. To good approximation, then, neutrino-nucleus reactions in the outer layers of the helium shell build up a supply of protons that are then captured during postshock nucleosynthesis by ^{18}O to make ^{15}N.

D. Neutrinos and other explosion energies

Figure 31 shows the final ^{15}N mass fraction in the helium shell for explosion calculations using reaction rates updated from Set 2 and with inclusion of neutrinos with the enhanced neutron and proton neutrino spallation on ^{16}O. The curves represent our best fits to the calculations of Ref. [4] in the helium shell.

As in Fig. 6, the peak in the ^{15}N mass fraction stays at roughly the same height but moves out in interior mass coordinate with increasing explosion energy. As with our previous calculations, this is due to the competition between

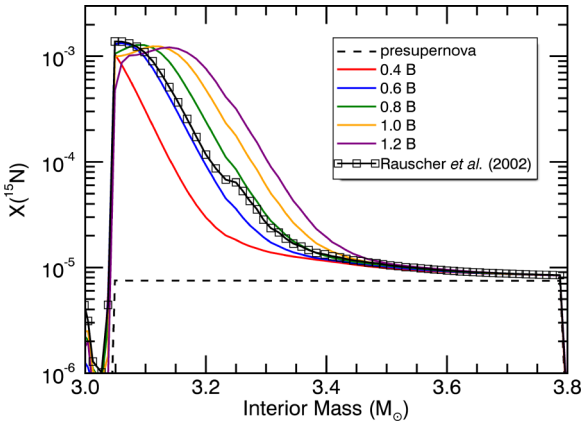

FIG. 31. (Color online) Final ^{15}N mass fraction as a function of interior mass coordinate 10^6 seconds after the explosion of s15a28 for the indicated explosion energies. These calculations included the effects of neutrino-nucleus interactions with the enhanced neutron and proton neutrino spallation on ^{16}O and the reaction rates were updated with rate data from Set 2. Also shown for comparison are the presupernova and postsupernova values from Ref. [4].

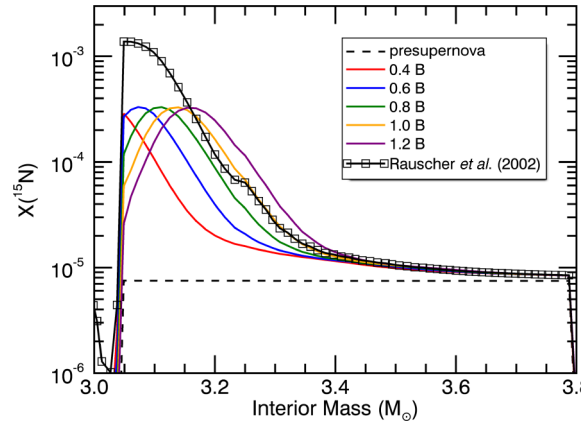

FIG. 32. (Color online) Final ^{15}N mass fraction as a function of interior mass coordinate 10^6 seconds after the explosion of s15a28 for the indicated explosion energies. These calculations included the effects of neutrino-nucleus interactions with the enhanced neutron and proton neutrino spallation on ^{16}O but the reaction rates were only those in REACLIBV2.0. Also shown for comparison are the presupernova and postsupernova values from Ref. [4].

^{15}N production and destruction. The higher peaks in Fig. 31 compared to Fig. 6 result from reaction rate differences discussed in Sec. IV.

Interestingly, the curves in Fig. 31 all tend to converge in the outer layers of the helium shell. This is due to the fact that production of ^{15}N is from ^{18}O$(p,\alpha)^{15}$N, with the protons largely produced before shock passage by neutrino-nucleus interactions. These interactions are independent of E, so all of the calculations began with the same initial proton mass fraction. For all explosion energies, the postshock temperature in the outer helium-shell layers became high enough to cause all of the protons to be consumed and thereby create ^{15}N.

None of our curves match that of Ref. [4] in the helium shell. This shows the limitation of our explosion model. We best fit the Ref. [4] results with our $E = 0.6$ B results in the inner part of the helium shell. At larger interior mass coordinate, however, the Ref. [4] results are better fit with a higher energy. From Fig. 4, we know that the shock is slowing as it passes through the helium shell and that it had been accelerating prior to reaching that shell. We infer that, in the full hydrodynamical models, the shock somewhat outran the ability of the postshock matter to homogenize its energy density as it reached the helium shell. This means that the energy density just behind the shock was probably somewhat less than the average postshock energy density. To some extent, this resulted in a lower peak temperature on shock passage, and our model reproduces that peak temperature with a lower explosion energy. As the shock then moved through the helium shell, it slowed, which may have allowed the energy density just behind the shock to catch up with the average energy density. The Ref. [4] calculation was for an explosion energy $E = 1.2$ B and, in fact, in the outer layers of the helium shell, our ^{15}N mass fraction best fits the Ref. [4] calculation for $E = 1.2$ B.

It is worth noting for our model that large differences in explosion energy correspond to relatively small differences in peak postshock temperature. For example, Eq. (7) shows that the peak postshock temperature behaves as $E^{1/4}$; thus, for a given zone, the peak postshock temperature for $E = 1.2$ B is only 19% higher than for $E = 0.6$ B.

Figure 32 is identical to Fig. 31 except that the reaction rates were not updated with rate data from Set 2. These results, then, are our best estimates for the ^{15}N mass fraction in the helium shell given current reaction rate data. Significantly, the peak ^{15}N mass fraction is $\sim 4\times$ lower than that of Ref. [4] due to reaction rate differences between REACLIBV2.0 and REACLIBV2.0 updated from Set 2.

VI. PRESOLAR GRAINS

Figure 33 shows overabundances (abundances relative to their solar values) for nitrogen, oxygen, and molybdenum isotopes resulting from our $E = 1.0$ B explosion of s15a28 with REACLIBV2.0 rates only. We note that, had we updated the rates with the Set 2 values, the ^{15}N overabundance peak would be $\sim 4\times$ higher. As we have seen, strong neutron capture by ^{18}F is the dominant production mechanism of ^{15}N in the peak region. Neutron capture also plays an important role in zones just inside those containing the most ^{15}N. Strong overabundance peaks of ^{95}Mo and ^{97}Mo in the interior mass range 2.8–2.9$M_\odot$ arise from the neutron burst (or n process) that occurs as the shock passes through these layers and liberates neutrons by ^{22}Ne$(\alpha,n)^{25}$Mg [20].

Figure 34 shows the mass fractions of ^{4}He, ^{18}O, and ^{22}Ne inside the presupernova star. Partial burning of ^{18}O to ^{22}Ne leaves a mix of both species in the helium-rich shell. Inside that shell, the conversion of ^{18}O to ^{22}Ne is complete. The ^{4}He is completely exhausted inside of $M_r \approx 2.8M_\odot$. A high postshock neutron density is thus achieved in the mass range $M_r \approx 2.8$–$3.0M_\odot$ by ^{22}Ne$(\alpha,n)^{25}$Mg and $M_r \approx 3.0$–$3.3M_\odot$ by ^{18}O$(\alpha,n)^{21}$Ne. Inside of $M_r \approx 2.8M_\odot$, the supply of ^{4}He is too low to create an explosive burst of neutrons and outside of $M_r \approx 3.3M_\odot$ the peak postshock temperature reached

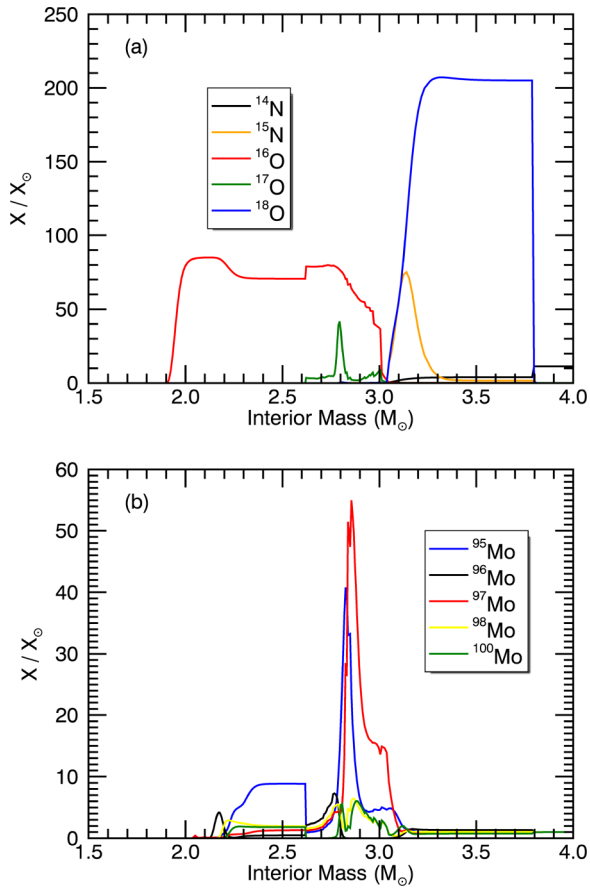

FIG. 33. (Color online) Overabundances of (a) nitrogen and oxygen isotopes and (b) molybdenum isotopes for the $E = 1.0$ B explosion of s15a28 with REACLIBV2.0 rates only. To avoid further clutter in the figure, we do not show the overabundances of ^{92,94}Mo, which peak around $M_r = 2M_\odot$ due to p-process nucleosynthesis there.

is too low. It is therefore not surprising that zones that create enrichments in ^{15}N and ^{95,97}Mo should lie near each other.

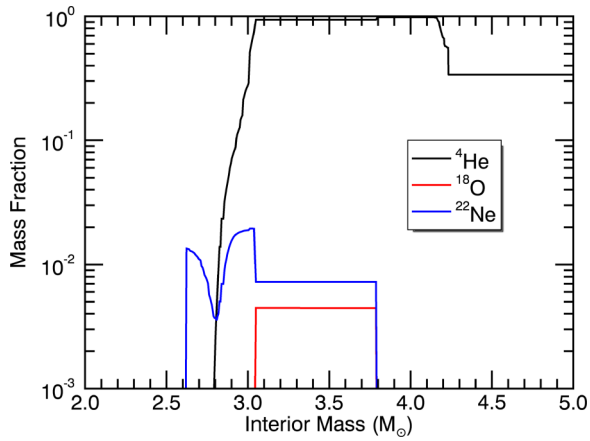

FIG. 34. (Color online) Mass fractions of ^{4}He, ^{18}O, and ^{22}Ne as a function of interior mass coordinate inside the presupernova star s15a28.

As discussed in the Introduction, low-density graphite grains show spatially correlated hot spots in ^{15}N and ^{18}O, which are most abundant in the inner part of the helium-rich ejecta from an exploding massive star. While enrichments in ^{95,97}Mo have not been observed in low-density supernova graphites, they have been found in supernova silicon carbide X (SiC X) grains [21]. These SiC X grains share a number of isotopic characteristics (e.g., ^{12}C richness and excesses in ^{44}Ca from *in situ* decay of ^{44}Ti) with low-density grains and may have formed in an analogous manner. Isotopic signatures thus clearly signal a role for the inner, helium-rich zones in massive star ejecta in the formation of supernova carbonaceous dust.

We note from Fig. 4 that the shock and, thus, postshock velocity of the ejecta slow down as the shock passes through the helium shell. This causes material in this shell to pile up and create a helium wall [22]. Such piling up could set the stage for grain growth. Interestingly, the ^{44}Ti that gives rise to the ^{44}Ca excesses and the ^{28}Si for production of the SiC X grains could either be implanted into the helium wall via metal-rich knots from the supernova interior [23] or created in the helium-rich layers themselves if the explosive burning is strong enough [24].

The helium-rich zones also have the property that they are the only ones in the stellar ejecta with C > O in abundance. Because the CO molecule is tightly bound, as the material in zones with C < O cools, it will tend to lock up carbon into CO and not make carbon dust. On the other hand, supernovas are profoundly radioactive, and Compton upscattered electrons from decay of abundant ^{56}Co can limit the buildup of CO and allow growth of carbon dust in environments with C < O [25–28]. The property that C > O is thus suggestive of the provenance of the grains but is perhaps not as definitive as the isotopic signatures.

VII. CONCLUSIONS

We have explored explosive nucleosynthesis of ^{15}N with a simple model of shock propagation through the outer layers of an initially $15M_\odot$ massive star model. We showed (cf. Figs. 7 and 18) that the main production pathway of ^{15}N in the inner part of the helium shell is the reaction sequence ^{14}N$(\alpha,\gamma)^{18}$F$(n,\alpha)^{15}$N while the main destruction of ^{15}N comes from ^{15}N$(p,\alpha)^{12}$C and ^{15}N$(\alpha,\gamma)^{19}$F. In the outer part of the helium shell, production of ^{15}N predominantly occurs via ^{18}O$(p,\alpha)^{15}$N, where the protons come from neutrino-nucleus interactions before and after shock passage. In zones inside the helium shell, the neutrino-nucleus interactions play a dominant role in ^{15}N production either by direct synthesis via spallation on ^{16}O in the C/O layers or, in the α-rich freeze-out layers, by initiating a charged-particle reaction sequence.

The competition between production and destruction gives rise to a peak structure of ^{15}N in the helium shell. Because of this competition, the location of the peak depends on the peak postshock temperature in each zone and, hence, on the explosion energy E; however, the height of the peak is nearly independent of E. This result allows us to conclude that the difference between the height of the helium-shell mass fraction peak in our calculations and those of Ref. [4] is not due to differing treatments of the explosion fluid dynamics

but rather to differences in the reaction rate data used. We confirm this by reproducing the Ref. [4] ^{15}N mass fraction peak height when we use rate data employed by those authors (our Set 2) for key reactions. From this, we conclude that the Ref. [4] ^{15}N mass fraction peak height would be $\sim 4\times$ lower if those calculations had used the REACLIBV2.0 reaction rate data (cf. Figs. 31 and 32). Those seeking to match nitrogen isotopic data in presolar grains with stellar model outputs should take this potential degree of variation into account.

The factor $\sim$4 difference in the helium-shell ^{15}N mass fraction peak between calculations with and without rate data updated from Set 2 arose mainly from four reactions: $^{14}\mathrm{N}(\alpha,\gamma)^{18}\mathrm{F}$, $^{18}\mathrm{F}(n,p)^{18}\mathrm{O}$, $^{15}\mathrm{N}(\alpha,\gamma)^{19}\mathrm{F}$, and $^{18}\mathrm{O}(\alpha,n)^{21}\mathrm{Ne}$. In the innermost regions of the helium shell, the last of these reactions, which produces the bulk of the neutrons during the explosive nucleosynthesis, does not play much of a role since the ^{18}F mass fraction is in steady state during the important phases of the burning. In layers outside these regions, however, the ^{18}F mass fraction is not in steady state, and the importance of the reaction grows. The $^{18}\mathrm{F}(n,p)^{18}\mathrm{O}$ reaction plays a role because it competes with $^{18}\mathrm{F}(n,\alpha)^{15}\mathrm{N}$ and because the protons it produces enhances the destruction of ^{15}N.

In the 1970s, difficulties with the then prevailing models for r-process nucleosynthesis led a number of workers to consider explosive burning in helium-rich layers of massive stars as the mechanism for production of the heavy neutron-rich isotopes in nature [29,30]. Subsequent work showed that, although a relatively high fluence of neutrons was released during the nucleosynthesis, the conditions were not right to produce a solarlike r-process abundance distribution but also that such nucleosynthesis could produce neutron-rich isotopes perhaps important for understanding meteoritic isotopic anomalies [31,32]. The heavy component of xenon (Xe-H) in meteoritic nanodiamonds may arise from such a neutron burst [33–36], and the usual isotopic molybdenum in presolar SiC X grains [21] almost certainly does [20]. Neutron burst nucleosynthesis may be responsible for the bulk of the early Solar System abundances of the short-lived radioactivities ^{60}Fe, ^{107}Pd, ^{129}I, and ^{182}Hf, whose presence in the early Solar System is inferred from isotopic anomalies in primitive meteorites (e.g., Ref. [37]). From the considerations in this paper, we conclude a significant component of ^{15}N in presolar supernova grains should also be classified as due to such nucleosynthesis.

While this paper has focused on ^{15}N, the codes and tools we have developed and made available are suitable for studying explosive nucleosynthesis of other isotopes in this or other stellar models. We encourage interested readers to try these codes and tools for their own purposes. We remind such readers that the Supplemental Material gives some details on how to obtain and compile the codes and how to reproduce the calculations and figures we show in this paper.

ACKNOWLEDGMENTS

This work was supported by NASA Grant No. NNX10AH78G. B.S.M. gratefully acknowledges the hospitality of the Hawaii Institute for Geophysics and Planetology at the University of Hawaii, Manoa, where some of this work was performed.

[1] D. D. Clayton and L. R. Nittler, Ann. Rev. Astron. Astrophys. **42**, 39 (2004).
[2] M. Jadhav, E. Zinner, S. Amari, T. Maruoka, K. K. Marhas, and R. Gallino, Geochim. Cosmochim. Acta **113**, 193 (2013).
[3] E. Groopman, T. Bernatowicz, and E. Zinner, Astrophys. J. Lett. **754**, L8 (2012).
[4] T. Rauscher, A. Heger, R. D. Hoffman, and S. E. Woosley, Astrophys. J. **576**, 323 (2002).
[5] W. M. Howard, W. D. Arnett, and D. D. Clayton, Astrophys. J. **165**, 495 (1971).
[6] M. Arnould and W. Beelen, Astron. Astrophys. **33**, 215 (1974).
[7] See Supplemental Material at http://link.aps.org/supplemental/10.1103/PhysRevC.89.025807 for instructions on downloading and installing the codes, running the calculations, and reproducing the figures in this paper.
[8] S. E. Woosley and T. A. Weaver, Astrophys. J. Suppl. **101**, 181 (1995).
[9] Available at http://sourceforge.net/p/nucnet-projects/wiki/Home
[10] Available at http://sourceforge.net/p/nucnet-tools
[11] L. I. Sedov, *Similarity and Dimensional Methods in Mechanics* (Academic Press, New York, 1959).
[12] M. Herant and S. E. Woosley, Astrophys. J. **425**, 814 (1994).
[13] R. H. Cyburt, A. M. Amthor, R. Ferguson, Z. Meisel, K. Smith, S. Warren, A. Heger, R. D. Hoffman, T. Rauscher, A. Sakharuk *et al.*, Astrophys. J. Suppl. **189**, 240 (2010).
[14] S. E. Woosley, D. H. Hartmann, R. D. Hoffman, and W. C. Haxton, Astrophys. J. **356**, 272 (1990).
[15] U. Giesen, C. P. Browne, J. Görres, J. G. Ross, M. Wiescher, R. E. Azuma, J. D. King, J. B. Vise, and M. Buckby, Nucl. Phys. A **567**, 146 (1994).
[16] S. Dababneh, M. Heil, F. Käppeler, J. Görres, M. Wiescher, R. Reifarth, and H. Leiste, Phys. Rev. C **68**, 025801 (2003).
[17] Y.-Z. Qian and S. E. Woosley, Astrophys. J. **471**, 331 (1996).
[18] B. S. Meyer, G. C. Mclaughlin, and G. M. Fuller, Phys. Rev. C **58**, 3696 (1998).
[19] L.-S. The, D. D. Clayton, L. Jin, and B. S. Meyer, Astrophys. J. **504**, 500 (1998).
[20] B. S. Meyer, D. D. Clayton, and L.-S. The, Astrophys. J. Lett. **540**, L49 (2000).
[21] M. J. Pellin, A. M. Davis, R. S. Lewis, S. Amari, and R. N. Clayton, in *Lunar and Planetary Institute Science Conference Abstracts*, Vol. 30 (Lunar and Planetary Institute, Houston, 1999), p. 1969.
[22] N. J. Hammer, H.-T. Janka, and E. Müller, Astrophys. J. **714**, 1371 (2010).
[23] A. V. Fedkin, B. S. Meyer, and L. Grossman, Geochim. Cosmochim. Acta **74**, 3642 (2010).
[24] M. Pignatari, M. Wiescher, F. X. Timmes, R. J. de Boer, F.-K. Thielemann, C. Fryer, A. Heger, F. Herwig, and R. Hirschi, Astrophys. J. Lett. **767**, L22 (2013).
[25] D. D. Clayton, W. Liu, and A. Dalgarno, Science **283**, 1290 (1999).

[26] D. D. Clayton, E. A.-N. Deneault, and B. S. Meyer, Astrophys. J. **562**, 480 (2001).
[27] E. A.-N. Deneault, D. D. Clayton, and A. Heger, Astrophys. J. **594**, 312 (2003).
[28] T. Yu, B. S. Meyer, and D. D. Clayton, Astrophys. J. **769**, 38 (2013).
[29] J. B. Blake and D. N. Schramm, Astrophys. J. **209**, 846 (1976).
[30] J. W. Truran, J. J. Cowan, and A. G. W. Cameron, Astrophys. J. Lett. **222**, L63 (1978).
[31] F.-K. Thielemann, M. Arnould, and W. Hillebrandt, Astron. Astrophys. **74**, 175 (1979).
[32] J. B. Blake, S. E. Woosley, T. A. Weaver, and D. N. Schramm, Astrophys. J. **248**, 315 (1981).
[33] D. Heymann and M. Dziczkaniec, in *Proceedings of the 10th Lunar and Planetary Science Conference*, Vol. 2 (A80-23617 08-91) (Pergamon Press, New York, 1979), pp. 1943–1959.
[34] D. Heymann and M. Dziczkaniec, in *Proceedings of the 11th Lunar and Planetary Science Conference*, Vol. 2 (A82-22296 09-91) (Pergamon Press, New York, 1980), pp. 1179–1213.
[35] D. Heymann, Astrophys. J. **267**, 747 (1983).
[36] W. M. Howard, B. S. Meyer, and D. D. Clayton, Meteoritics **27**, 404 (1992).
[37] G. R. Huss, B. S. Meyer, G. Srinivasan, J. N. Goswami, and S. Sahijpal, Geochim. Cosmochim. Acta **73**, 4922 (2009).
[38] G. R. Caughlan and W. A. Fowler, At. Data Nucl. Data Tables **40**, 283 (1988).
[39] W. A. Fowler, G. R. Caughlan, and B. A. Zimmerman, Ann. Rev. Astron. Astrophys. **13**, 69 (1975).
[40] F.-K. Thielemann, M. Arnould, and J. W. Truran, in *Advances in Nuclear Astrophysics*, edited by E. Vangioni-Flam, J. Audouze, M. Cassé, J.-P. Chieze, and J. Tran Thahn Van (Editions Frontières, Gif-sur-Yvette, 1987), p. 525.
[41] F.-K. Thielemann (1995), reaction rate library REACLIB.
[42] G. R. Caughlan, W. A. Fowler, M. J. Harris, and B. A. Zimmerman, At. Data Nucl. Data Tables **32**, 197 (1985).
[43] R. Longland, C. Iliadis, A. E. Champagne, J. R. Newton, C. Ugalde, A. Coc, and R. Fitzgerald, Nucl. Phys. A **841**, 1 (2010).
[44] C. Iliadis, R. Longland, A. E. Champagne, A. Coc, and R. Fitzgerald, Nucl. Phys. A **841**, 31 (2010).
[45] C. Iliadis, R. Longland, A. E. Champagne, and A. Coc, Nucl. Phys. A **841**, 251 (2010).
[46] C. Iliadis, R. Longland, A. E. Champagne, and A. Coc, Nucl. Phys. A **841**, 323 (2010).
[47] I. Dillmann, M. Heil, F. Kaeppeler, R. Plag, T. Rauscher, and F.-K. Thielemann, in AIP Conf. Proc. No. 819 (AIP, New York, 2007), p. 123.
[48] V. Landre, N. Prantzos, P. Aguer, G. Bogaert, A. Lefebvre, and J. P. Thibaud, Astron. Astrophys. **240**, 85 (1990).
[49] P. J. LeBlanc, G. Imbriani, J. Görres, M. Junker, R. Azuma, M. Beard, D. Bemmerer, A. Best, C. Broggini, A. Caciolli *et al.*, Phys. Rev. C **82**, 055804 (2010).
[50] T. Rauscher, J. H. Applegate, J. J. Cowan, F.-K. Thielemann, and M. Wiescher, Astrophys. J. **429**, 499 (1994).
[51] T. Rauscher, NON-SMOKER Hauser Feshbach rates with Audi-Wapstra masses, private communication to the authors of Ref. [13].
[52] R. V. Wagoner, Astrophys. J. Suppl. **18**, 247 (1969).
[53] M. Wiescher and K.-U. Kettner, Astrophys. J. **263**, 891 (1982).